

ALICE-ANA-2018-xxx  
March 17, 2018

## D mesons in jets in p–Pb collisions: preliminary figures for QM 2018

Salvatore Aiola<sup>1</sup>, Fabio F. Colamaria<sup>2</sup>, Andrea Rossi<sup>3</sup>, Antonio C. O. da Silva<sup>4,5</sup>, Barbara A. Trzeciak<sup>4</sup>

1. Yale University, USA
2. University of Bari and INFN, Italy
3. University of Padova and INFN, Italy
4. Utrecht University, Netherlands
5. University of São Paulo, Brazil

Email: [barbara.antonina.trzeciak@cern.ch](mailto:barbara.antonina.trzeciak@cern.ch)

### Abstract

Open heavy flavors (D, B) are born from the fragmentation of heavy quarks ( $c$ ,  $b$ ) which are produced in hard scatterings possible only at the beginning of heavy-ion collisions. Minimal effects of Quark-Gluon Plasma (QGP) on the production of heavy quarks allow for a simpler theoretical description. Their negligible annihilation rate allows us to measure them and study their energy loss mechanism during their travel through the QGP. Upon colliding, partons in opposing high-energy beams can scatter violently to produce correlated showers of particles, or jets. These are expected to be modified by the interaction of the scattered partons with the surrounding QGP. Measuring D mesons in jets is therefore essential in understanding QGP. A precise, quantitative understanding of charmed jets is unavailable in the framework of perturbative QCD (pQCD). Charm content is available from prompt production:  $gg(q\bar{q}) \rightarrow c\bar{c}$ , and from the parton shower of gluons and light quarks. The aim of the analysis is to extract the  $p_T$  spectrum of the D-tagged jets. We identify D-meson candidates via their hadronic decay channels using topological selections and particle identification. These candidates are combined with the other charged tracks reconstructed by the central tracking system, using the anti- $k_T$  jet-finding algorithm. We extract the yield of D-tagged jets through their invariant mass analysis in bins of D  $p_T$  and get their jet  $p_T$  spectra. At the Quark Matter 2018, we show new preliminary results from the p-Pb analysis of the  $D^0$ -tagged jets, and  $D^{*\pm}$ -tagged jets.



## Contents

<b>1</b>	<b>Software</b>	<b>3</b>
<b>2</b>	<b>Dataset and Event Selection</b>	<b>3</b>
2.0.1	Monte Carlo productions . . . . .	4
<b>3</b>	<b>D-Meson Selection</b>	<b>4</b>
3.1	Particle Identification . . . . .	4
<b>4</b>	<b>Jet Reconstruction</b>	<b>5</b>
4.1	Jet Selection . . . . .	5
<b>5</b>	<b>Raw Yield Extraction</b>	<b>5</b>
5.1	Direct Jet- $p_T$ Extraction Method . . . . .	6
5.2	Side-Band Subtraction Method . . . . .	7
5.3	Method Comparison . . . . .	10
<b>6</b>	<b>Efficiency Correction Procedure</b>	<b>14</b>
6.1	Reconstruction Efficiency . . . . .	14
6.2	Efficiency-Corrected Yields . . . . .	14
6.3	Method Comparison (Efficiency-Corrected Yields) . . . . .	15
<b>7</b>	<b>Underlying Event (p–Pb analysis)</b>	<b>18</b>
7.1	Average Background Momentum Density . . . . .	18
7.2	Jet Background Fluctuations . . . . .	18
<b>8</b>	<b>Jet Momentum Detector Response</b>	<b>20</b>
8.1	Detector Response Matrix . . . . .	20
<b>9</b>	<b>Feed-Down Correction</b>	<b>21</b>
9.1	Monte Carlo Simulation . . . . .	21
9.2	Feed-Down Subtraction . . . . .	22
<b>10</b>	<b>Unfolding</b>	<b>24</b>
<b>11</b>	<b>Systematic Uncertainties</b>	<b>25</b>
11.1	Raw Yield Extraction . . . . .	25
11.2	D-Meson Selection Cuts . . . . .	26

---

11.3	B Feed-Down Correction . . . . .	26
11.4	Unfolding . . . . .	28
11.5	Background fluctuation matrix . . . . .	29
11.6	Tracking Efficiency . . . . .	30
11.7	$p_T$ Shape of the Monte Carlo Spectrum . . . . .	31
11.8	Summary of Systematic Uncertainties . . . . .	33
<b>12</b>	<b>Results</b>	<b>34</b>
12.1	Monte Carlo Simulations . . . . .	35
12.1.1	Effect of the $p_{T,D}$ Cut . . . . .	36
<b>13</b>	<b>Preliminary Figures</b>	<b>36</b>

## 1 Software

The main analysis tasks (C++ classes) used in the analysis are in the PWGJE library of the AliPhysics software package:

- AliAnalysisTaskSEDmesonsFilterCJ (filters D mesons and creates a set of particles with the D meson instead of the daughters);
- AliAnalysisTaskFlavourJetCorrelations (correlates each D meson found with a jet);
- AliEmcalJetTask ;
- AliAnalysisTaskRhoSparse.

The AliPhysics version used for this analysis is the analysis tag: vAN-20170826 (with AliRoot v5-09-14-1).

The task used for this analysis generates a multiple axis histogram (THnSparse) that keeps information about:  $z_{||}$ , jet  $p_T$ , D-meson  $p_T$  and D-meson invariant mass.

The post-processing includes: projection of the THnSparse onto lower-dimensional histograms, raw signal extraction, response matrix generation, unfolding, B feed-down correction and the final plotting. The post-processing is relatively light-weight and is performed directly in a personal computer. This code is written using the C++ with ROOT.

## 2 Dataset and Event Selection

For this analysis we use the data collected by ALICE in 2016 during the Minimum Bias period of the p–Pb collisions at  $\sqrt{s_{NN}} = 5.02$  TeV. This data corresponds to the following data taking periods: LHC16q and LHC16t pass1, FAST and CENT\_woSDD productions were merged, the total number of events is 603.1 M (after all the selections outlined below) out of 834.5 M analysed. The complete list of runs used in this analysis are:

LHC16q: 265525, 265521, 265501, 265500, 265499, 265435, 265427, 265426, 265425, 265424, 265422, 265421, 265420, 265419, 265388, 265387, 265385, 265384, 265383, 265381, 265378, 265377, 265344, 265343, 265342, 265339, 265338, 265336, 265335, 265334, 265332, 265309  
 LHC16t: 267166, 267165, 267164, 267163

Events were selected using the event selection kINT7. Note that the analysis is performed in AOD, where the beam-gas and gas-gas events have been filtered out. Events were further filtered using the Physics Selection, and selection provided by:

- AliAnalysisTaskEmcal::IsEventSelected(), which rejects events based on event vertex quality, in particular requiring a reconstructed vertex position not farther than 10 cm from the center of the detector along the beam axis; and a distance between the SPD vertex and the V0 vertex not larger than 0.5 cm
- AliRDHFCutsDStartoKpipi::IsEventSelected(AliEvent\*), which rejects events for D\* candidates based on event vertex quality and pileup
- AliRDHFCutsD0toKpi::IsEventSelected(AliEvent\*), which rejects events for D<sup>0</sup> candidates based on event vertex quality and pileup.

Results shown below come from the LEGO trains HFCJ\_pPb:

343 (LHC16q\_pass1\_FAST), 344 (LHC16q\_pass1\_CENT\_woSDD), 345 (LHC16t\_pass1\_FAST) and 346 (LHC16t\_pass1\_CENT\_woSDD).

### 2.0.1 Monte Carlo productions

For this analysis the Monte Carlo production LHC17d2a\_fast\_new has been used, anchored to the 2016 p–Pb data taking periods LHC16q and LHC16t and the FAST production. The FAST production simulation is used to corrected the data sample, which is merged FAST+CENT\_woSDD, assuming that efficiencies are detector response are the same for both. The simulations uses PYTHIA6 with the Perugia2011 tune as particle generator at  $\sqrt{s} = 5.02$  TeV. If  $N_{coll} > 1$ , the event generated by Hijing is also embedded. The charm content has been enhanced by requesting a  $c\bar{c}$  in 50% of the events and a  $b\bar{b}$  in the remaining half. Furthermore, all D mesons are forced to decay hadronically. This MC production is used to compute the D-meson efficiency with jets, acceptance corrections and a response matrix of D-tagged jets with prompt and non-prompt  $D^{*\pm}$ :  $c, b \rightarrow D^{*\pm}$ .

Results shown below come from the LEGO trains HFCJ\_pPb\_MC: **XX77** (full simulation), and 76 (only Pythia part of the simulation).

## 3 D-Meson Selection

The  $D^{*\pm}$  mesons were reconstructed through their hadronic decay channels [1]:

$$\begin{aligned} D^0(\bar{D}^0) &\rightarrow K^\pm + \pi^\mp, \text{ BR} = 3.93 \pm 0.04\% \\ D^{*\pm} \rightarrow D^0 + \pi^\pm &\rightarrow K^\pm + \pi^\mp + \pi^\pm, \text{ BR} = 67.7 \pm 0.5\%, 3.93 \pm 0.04\% \end{aligned}$$

The selection strategy is based on the topological displacement of the secondary vertex from the primary vertex due to their relatively large lifetime.

The candidate vertices are read from the AOD friend chain `AliAOD.VertexingHF.root`. A list of topological and kinematic cuts applied for  $D^{*\pm}$  in p–Pb collisions at  $\sqrt{s_{NN}} = 5.02$  TeV can be found in Table 1 and in Table 2 for  $D^0$  in the same p–Pb collisions at  $\sqrt{s_{NN}} = 5.02$  TeV. The same quality track selection on the decay products used for the D-meson spectra analysis of the same datasets has been used in this analysis. For the final jet spectrum we will apply  $p_{T,D} > 3$  GeV/c on the D mesons. The accepted  $|y_D|$  range is  $p_T$ -dependent, with the upper limit growing from 0.5 to 0.8 at  $p_T = 5$  GeV/c.

Table 1:  $D^{*\pm}$  cuts for p–Pb collisions at  $\sqrt{s_{NN}} = 5.02$  TeV.

$p_{T,D^{*\pm}}$ (GeV/c)	0.5–1	1–2	2–3	3–4	4–5	5–6	6–7	7–8	8–10	10–12	12–16	16–24	24–36
$\Delta M_{D^{*\pm}}$ (GeV/ $c^2$ )	0.03	0.032	0.032	0.032	0.032	0.036	0.036	0.036	0.05	0.05	0.094	0.094	0.7
DCA (cm)	0.0315	0.025	0.03	0.03	0.035	0.04	0.08	0.12	0.12	0.12	0.2	0.2	0.5
$\cos(\theta^*)$	0.9	0.8	0.8	0.8	0.9	1	1	1	1	1	1	1	1
$p_{T,K}$ (GeV/c)	0.5	1	1	1	1	1	1	1	1	1	0.3	0.3	0
$p_{T,\pi}$ (GeV/c)	0.5	1	1	1	1	1	1	1	1	1	0.3	0.3	0
$d_0^K$ (cm)	0.1	0.1	0.1	0.1	0.1	0.1	0.1	0.1	0.1	0.1	0.2	0.2	999
$d_0^\pi$ (cm)	0.1	0.1	0.1	0.1	0.1	0.1	0.1	0.1	0.1	0.1	0.2	0.2	999
$d_0^K \cdot d_0^\pi$ ( $10^{-4}$ cm $^2$ )	-3	-2	-2.5	-1.3	-0.38	0.44	5	5	100	100	500	1000	1000
$\cos(\theta_{\text{point}})$	0.8	0.9	0.9	0.87	0.86	0.83	0.76	0.76	0.68	0.68	0.60	-1	-1
$\cos(\theta_{\text{point},xy})$	-	0.97	-	-	-	-	-	-	-	-	-	-	-
$L_{xy}/\sigma_{L_{xy}}$ (cm)	4	3.5	4	3.5	3	2.5	1.5	1	0	0	0	0	0

### 3.1 Particle Identification

The Particle Identification (PID) of pions and kaons was performed using the information of the specific energy loss in the TPC and the time of flight provided by the TOF detector. In order to identify a track as a pion or a kaon its TPC  $dE/dx$  and/or time-of-flight were required to be within  $3\sigma$  of the expected values. Tracks with no TOF information were identified using only the TPC. When PID is inconclusive

Table 2:  $D^0$  cuts for p–Pb collisions at  $\sqrt{s_{\text{NN}}} = 5.02$  TeV.

$p_{T,D^0}$ (GeV/c)	0.5–1	1–2	2–3	3–4	4–5	5–6	6–7	7–8	8–10	10–12	12–16	16–24	24–36
$\Delta M_{D^0}$ (GeV/ $c^2$ )	0.4	0.4	0.4	0.4	0.4	0.4	0.4	0.4	0.4	0.4	0.4	0.4	0.4
DCA (cm)	0.03	0.03	0.03	0.03	0.03	0.03	0.03	0.03	0.03	0.03	0.03	0.03	0.03
$\cos(\theta^*)$	0.8	0.8	0.8	0.8	0.8	0.8	0.8	0.8	0.9	0.9	1	1	1
$p_{T,K}$ (GeV/c)	0.5	0.5	0.7	0.7	0.7	0.7	0.7	0.7	0.7	0.7	0.7	0.7	0.7
$p_{T,\pi}$ (GeV/c)	0.5	0.5	0.7	0.7	0.7	0.7	0.7	0.7	0.7	0.7	0.7	0.7	0.7
$d_0^K$ (cm)	0.1	0.1	0.1	0.1	0.1	0.1	0.1	0.1	0.1	0.1	0.1	0.1	0.1
$d_0^\pi$ (cm)	0.1	0.1	0.1	0.1	0.1	0.1	0.1	0.1	0.1	0.1	0.1	0.1	0.1
$d_0^K \cdot d_0^\pi$ ( $10^{-4}$ cm $^2$ )	-5	-3.5	-3	-3	-1.5	-1	-0.8	-0.8	-0.5	-0.5	1	1	1
$\cos(\theta_{\text{point}})$	0.95	0.95	0.95	0.95	0.95	0.95	0.95	0.95	0.95	0.95	0.95	0.90	0.90
$L_{xy}/\sigma_{L_{xy}}$ (cm)	5	5	5	5	5	4	4	4	3	3	3	3	3

and neither the pion nor the kaon hypothesis can be excluded, tracks compatible with both the hypotheses were retained for analysis.

As a result, for the decay  $D^0(\bar{D}^0) \rightarrow K^\pm + \pi^\mp$ , the  $(K\pi)$  pair is counted twice with the two possible mass assignments. If the pair does not correspond to a real D meson, it would add two background entries in the invariant mass histogram, else it counts a signal plus a background entry. The misidentification rate (i.e. cases in which the wrong mass hypothesis is accepted while the correct one is rejected) is very small. In this case the signal D meson is lost and the entry contributes to the background in the invariant mass histogram. In the following  $D^0$  analysis,  $D^0$  reflections are defined as pion-kaon pairs that come from the decay of a real  $D^0$ , but with the reflected mass hypothesis.

## 4 Jet Reconstruction

The FASTJET[2] package was used to reconstruct the jets. In particular, the anti- $k_T$  algorithm [3] was employed to reconstruct signal jets. This algorithm is infrared-safe (not sensitive to low energy radiations) and collinear-safe (not sensitive to collinear particle splitting). A resolution parameter of  $R = 0.4$  was used for  $D^{*\pm}$  in p–Pb and  $R = 0.3$  was used for  $D^0$  in p–Pb. In the p–Pb analysis, the  $k_T$  algorithm [4] was employed to estimate the background. For this analysis, only charged tracks are used to reconstructed the jets (*charged jets*).

The set of tracks given as input to the jet finder has the D-meson daughters replaced by the 4-momentum of the D-meson candidate (sum of the 4-momenta of the daughters). The procedure is repeated independently for each D-meson candidate in each event, i.e. each candidate is treated as if it were the only one in the event, then (if there is more than one candidate) the procedure is repeated for each candidate one by one. This is done because two (or even more) candidates can share the same daughter.

### 4.1 Jet Selection

Tracks with  $p_T > 0.15$  GeV/ $c$  and  $|\eta| < 0.9$  were included in the jet finding. Reconstructed jets with the axis not satisfying  $|\eta_{\text{jet}}| < 0.9 - R$  were rejected. **i have to check**

## 5 Raw Yield Extraction

We have implemented two methods to extract the D-tagged jet  $p_T$  distribution. In both the methods, the signal in the  $D^{*\pm}$  invariant mass distribution is fit with a Gaussian distribution for the signal and the following function for the background:

$$f_{\text{bkg}}(m) = a(m - m_\pi)^{0.5} \exp(b(m - m_\pi)), \quad (1)$$

where  $m$  is the invariant mass,  $a$  and  $b$  are free parameters of the fit.

**Direct jet  $p_T$  extraction** The invariant mass distribution of the D-meson candidates is built for each  $p_{T,\text{chjet}}$  bin and the signal is extracted directly from the fit parameters.

**Side-band subtraction in D-meson  $p_T$  bins** The invariant mass distribution of the D-meson candidates is built for each  $p_{T,D}$  bin and the D-meson candidates that belong to the bins in the signal region  $3\sigma$  around the peak position) are used to build the peak-region jet  $p_T$  distribution; in order to remove the contribution of D-meson background, the jet  $p_T$  distribution corresponding to the side-band region (between  $-8\sigma$  and  $-5\sigma$  from the left-hand side of the  $D^{*\pm}$  peak and between  $5\sigma$  and  $13\sigma$  on the right-hand side) is taken and normalized to the background integral in the signal region, estimated from the fit.

For  $D^0$  the fit is performed using a Gaussian distribution for the signal and a power function for the background:

$$f(m) = Ce^{-(\frac{m-m_0}{2\sigma})^2} + am^b, \quad (2)$$

where  $m$  is the invariant mass,  $a$ ,  $b$ ,  $C$ ,  $m_0$ ,  $\sigma$  are free parameters.

In addition, the “reflection” templates are extracted from the charm-enhanced MC production. The invariant mass distributions for the reflection templates are shown in Fig. ?? and in Fig. ??.

### 5.1 Direct Jet- $p_T$ Extraction Method

The D-meson invariant mass is analyzed for each bin of jet  $p_T$ . The D-tagged jet raw yields and the relative uncertainties are extracted from the integral of the Gaussian fit function in the signal regions. The invariant mass distributions in bins of jet  $p_T$  for  $D^{*\pm}$  in p-Pb are shown in Fig. 1.

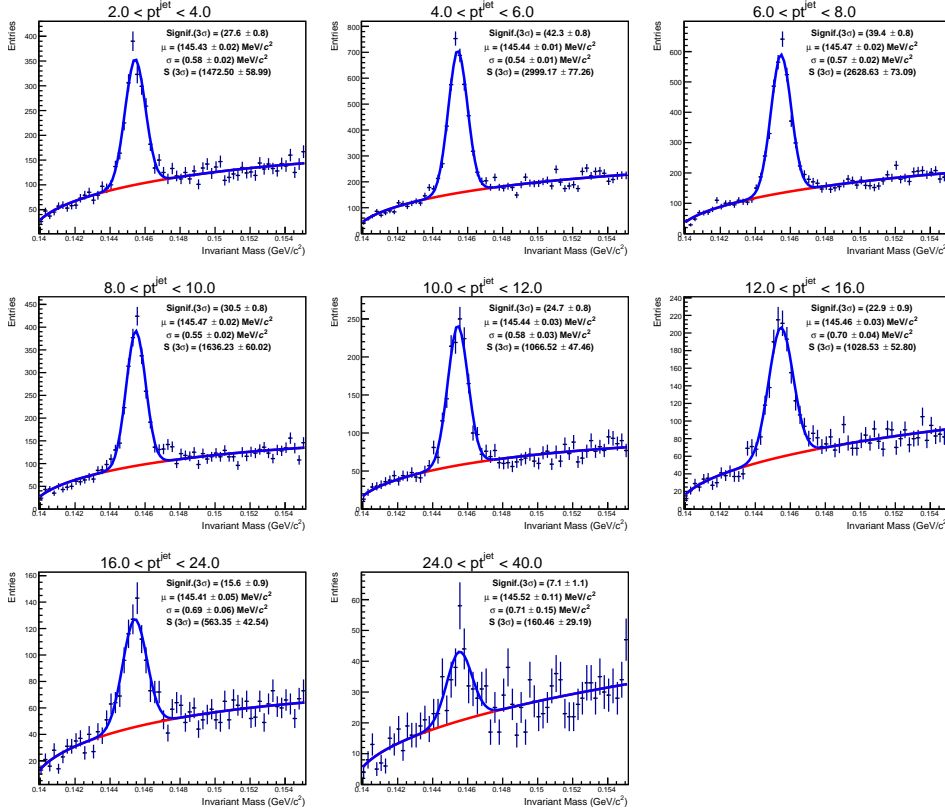


Fig. 1:  $D^{*\pm}$ -jet signal extraction in bins of jet transverse momentum in p-Pb collisions at  $\sqrt{s_{NN}} = 5.02$  TeV (raw yields). D mesons are required to have  $p_T > 3$  GeV/c.



Figure 2 shows a summary of the raw signal extraction: yield, relative statistical uncertainty, signal / background ratio and significance.

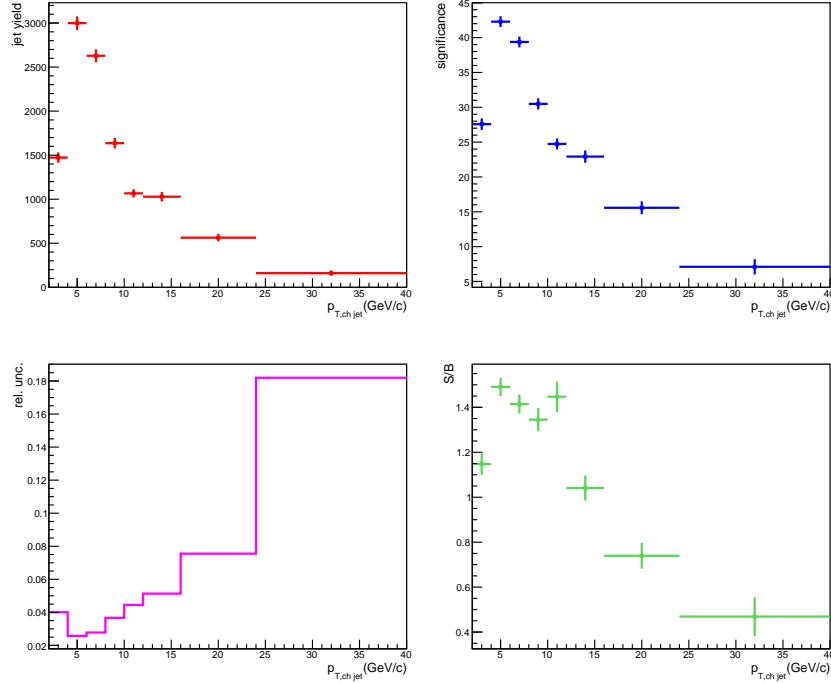


Fig. 2:  $D^{*\pm}$ -jet raw signal extraction in p–Pb collisions at  $\sqrt{s} = 5.02$  TeV for  $p_{T,D} > 3$  GeV/ $c$  with the direct jet- $p_T$  extraction method in bins of  $p_{T, \text{ch jet}}$ .

The invariant mass distributions shown here are not corrected for the reconstruction efficiencies. This step is discussed in Sec. 6.1.

The jet  $p_T$  bins are selected so that the significance of the  $D$  signal is above  $5\sigma$ . The reason of the  $D^{*\pm}$  signal visible in the Fig. 1 below  $p_{T, \text{jet}}$  of 3 GeV/ $c$  despite the  $p_{T,D}$  cut above 3 GeV/ $c$  is a subtraction of the jet background, as it is described in the Sec. 7.1.

## 5.2 Side-Band Subtraction Method

The  $D$ -meson invariant mass is analyzed for each bin of  $D$ -meson  $p_T$ . The  $D$ -meson candidates in the signal region ( $3\sigma$  around the peak) are used to build a jet  $p_T$  distribution, which comprises both signal and background  $D$ -meson candidates. Another jet  $p_T$  distribution is built using candidates with invariant mass that is between  $-8\sigma$  and  $-5\sigma$  on the left-hand side of the  $D^{*\pm}$  peak and between  $5\sigma$  and  $13\sigma$  on the right-hand side. For  $D^0$  the background region is between  $5\sigma$  and  $9\sigma$  from the peak. The normalization is done using the information of the fit integrating the background function inside the signal area. This is done separately and independently for each  $p_{T,D}$  bin.

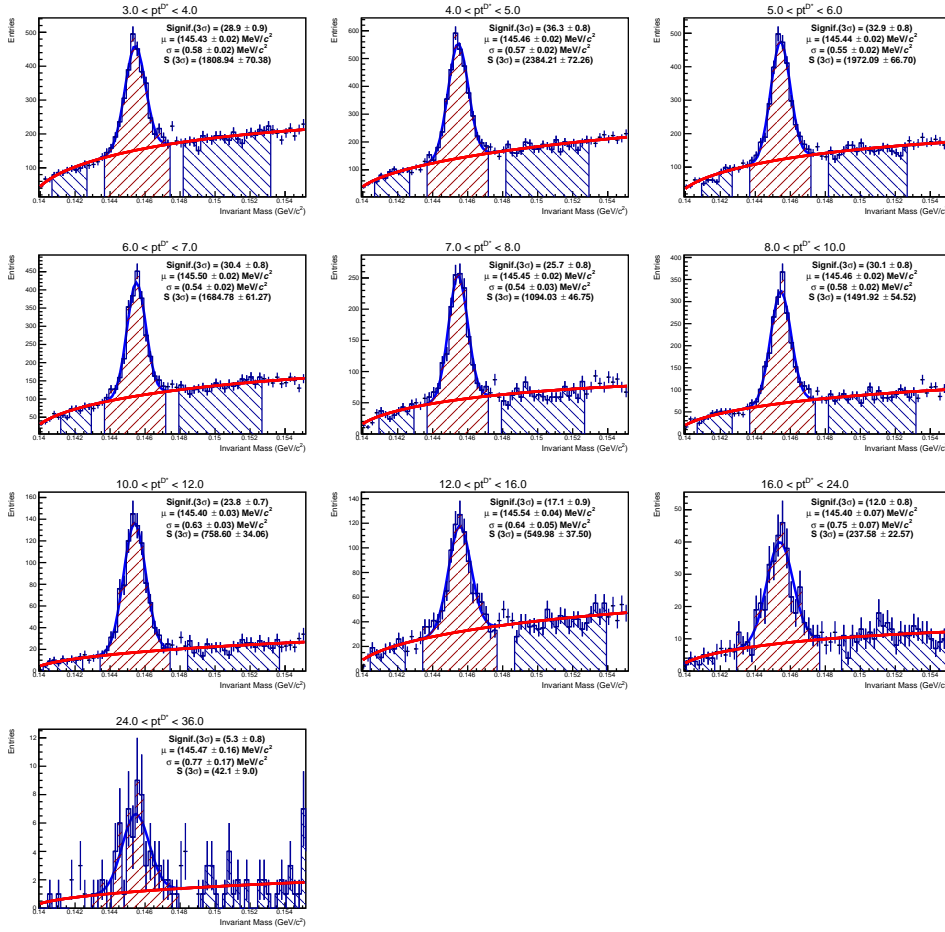


Fig. 3:  $D^{*\pm}$  signal extraction in bins of D-meson transverse momentum in p-Pb collisions at  $\sqrt{s_{NN}} = 5.02$  TeV (raw yields).

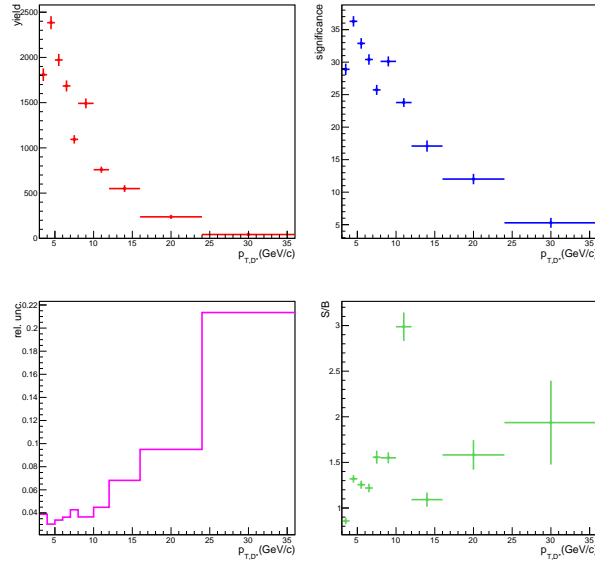


Fig. 4:  $D^{*\pm}$ -jet raw signal extraction in p-Pb collisions at  $\sqrt{s_{NN}} = 5.02$  TeV for  $p_{T,D} > 3$  GeV/c with the Side Band method.

The invariant mass distributions in bins of D-meson  $p_T$  are shown in Fig. 3 for  $D^{*\pm}$  and in Fig. 5 for

$D^0$  where the signal region is shown as the red shaded area, and the background region is depicted as the blue shaded area. Also shown in Fig. 5 are reflections for  $D^0$  in green, and their ratio over signal is shown in Fig. ??

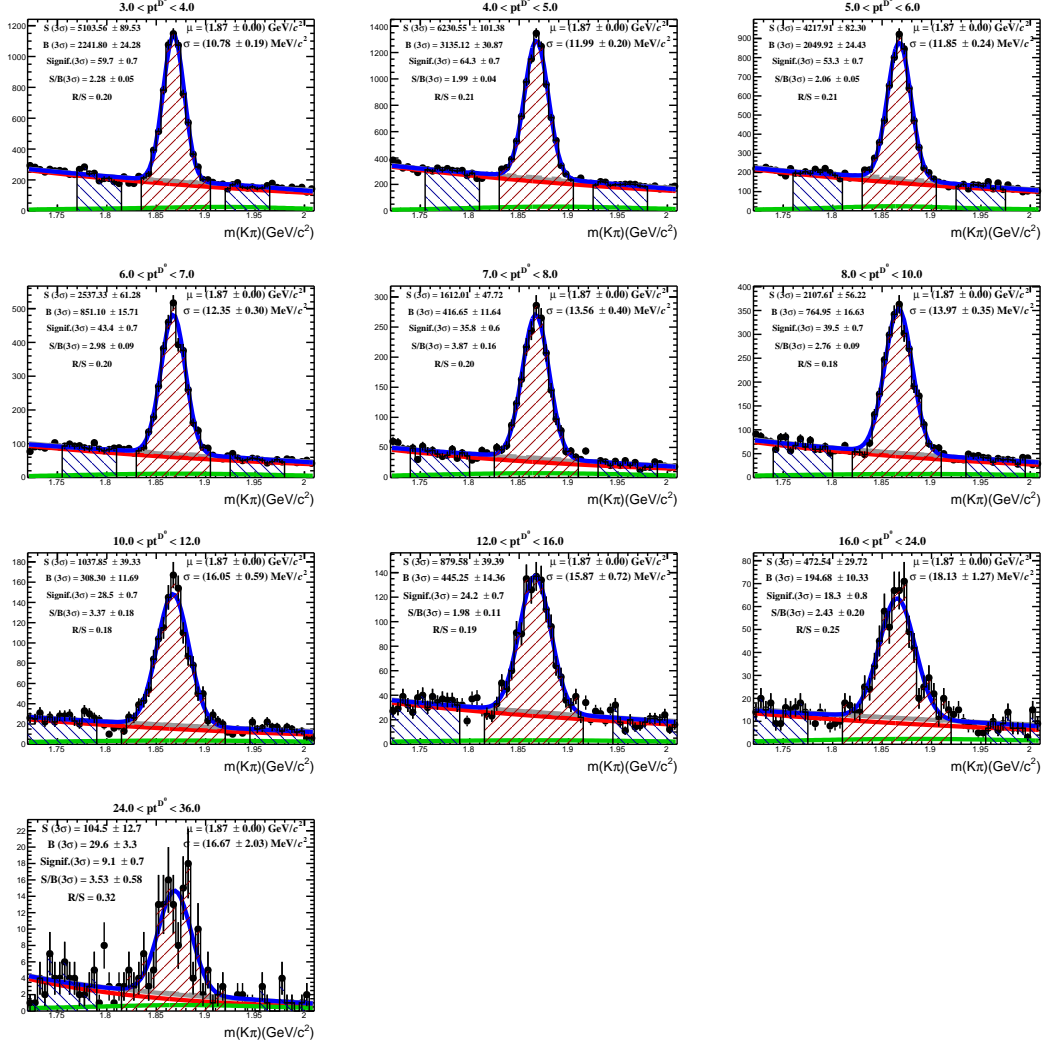


Fig. 5:  $D^0$ -jet signal extraction in bins of jet transverse momentum in p–Pb collisions at  $\sqrt{s_{NN}} = 5.02$  TeV (raw yields). D mesons are required to have  $p_T > 3$  GeV/c. Reflections shown by green curve add with the combinatorial background (red curve) to give the overall background in grey.

The jet  $p_T$  distributions for  $D^{*\pm}$  are shown in Fig. 8 and for  $D^0$  in Fig. 10, along with the jet  $p_T$  distributions for the background region. Then the background distributions are subtracted from the signal distributions and raw jet  $p_T$  distributions are obtained in each D  $p_T$  bin, as it is shown also in Fig. 8 for  $D^{*\pm}$  and in Fig. 10 for  $D^0$ . Figure 9 shows the sum of the jet  $p_T$  distributions for  $D^{*\pm}$ -jets without a correction for the D meson efficiency and rebinning. Figure ?? shows the same for  $D^0$ -jets.

Figures 4 and 6 show a summary of the raw signal extraction: yield, relative statistical uncertainty, signal / background ratio and significance, for  $D^{*\pm}$  and  $D^0$  respectively.

In order to obtain the final jet  $p_T$  spectrum, the distributions in each D  $p_T$  bin need to be corrected for the D efficiency and finally summed up. The corrections will be discussed in Section 6.1.

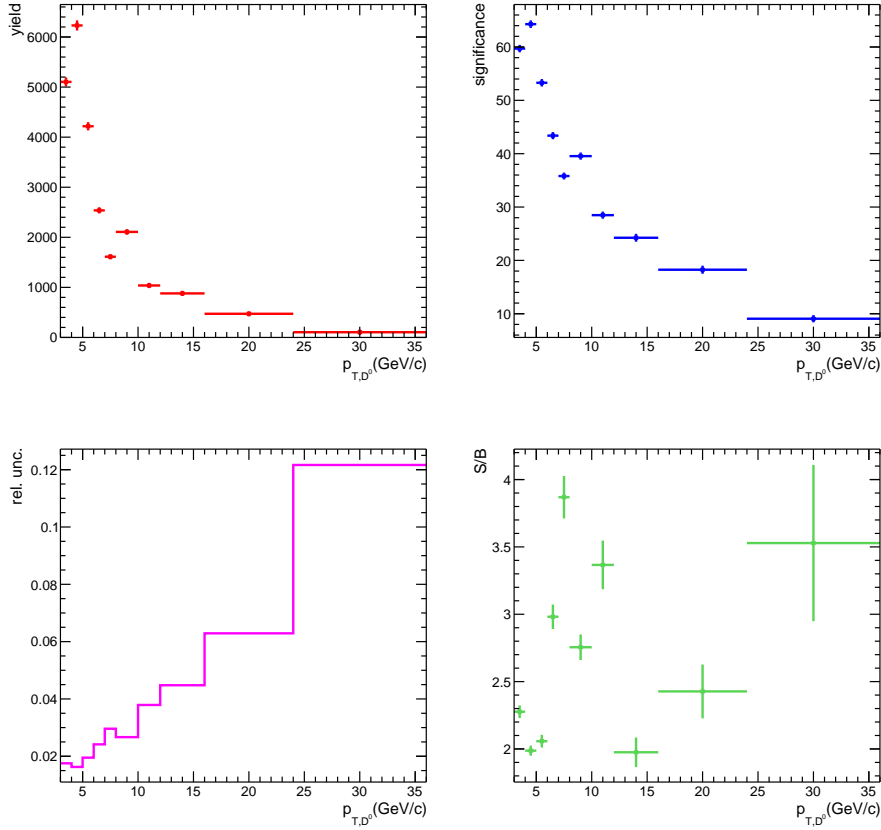


Fig. 6:  $D^0$ -jet raw signal extraction in p-Pb collisions at  $\sqrt{s_{NN}} = 5.02$  TeV for  $p_{T,D} > 3$  GeV/c with the Side Band method.

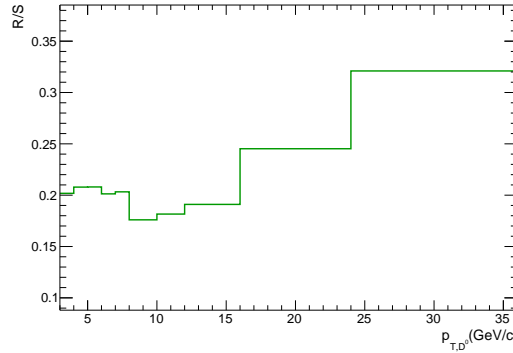


Fig. 7:  $D^0$ -jet raw signal extraction, reflections over signal ratio, in p-Pb collisions at  $\sqrt{s_{NN}} = 5.02$  TeV for  $p_{T,D} > 3$  GeV/c with the Side Band method.

### 5.3 Method Comparison

Figure 11 shows a comparison of the raw yields (without the D-reconstruction efficiency applied). Jet  $p_T$  spectra are checked with two cuts on the D-meson  $p_T$ :  $p_{T,D} > 2$  GeV/c and  $p_{T,D} > 3$  GeV/c. Both agree with each other as it is seen in Fig. 11. However, it is more important to cross-check the two methods with different  $p_{T,D}$  cuts after the efficiency correction is applied, as the background at low  $p_{T,D}$  influences the analysis more, as it is shown later.

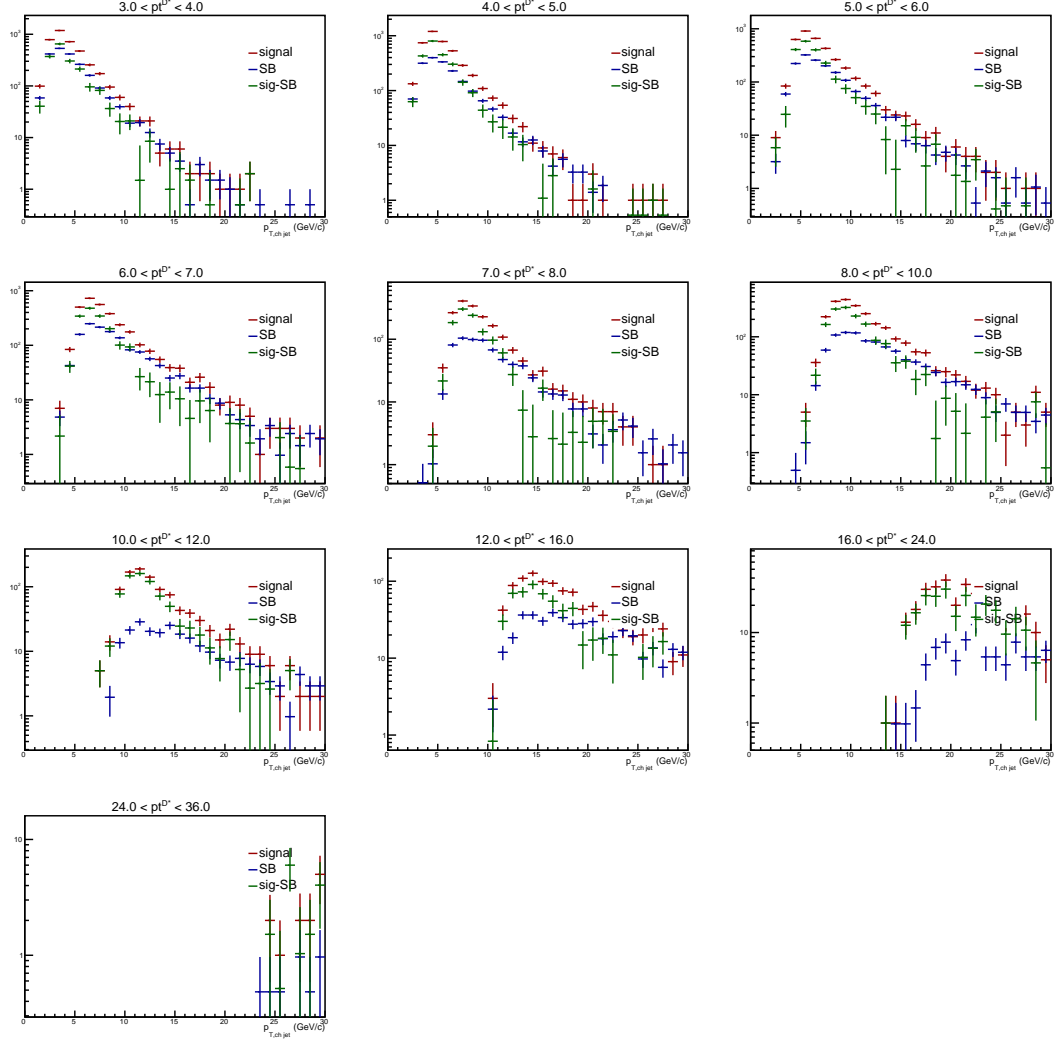


Fig. 8: Raw jet  $p_T$  distributions in bins of  $D^{*\pm}$  transverse momentum in p-Pb collisions at  $\sqrt{s_{NN}} = 5.02$  TeV.

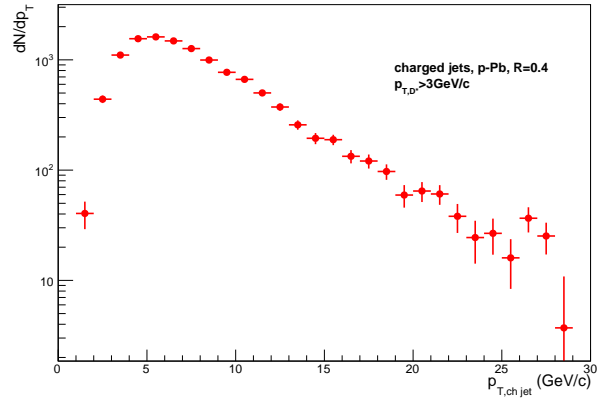


Fig. 9: Total raw jet  $p_T$  distributions for  $D^{*\pm}$  in p-Pb collisions at  $\sqrt{s_{NN}} = 5.02$  TeV, obtained summing together all the  $D^{*\pm}$   $p_T$  bins.

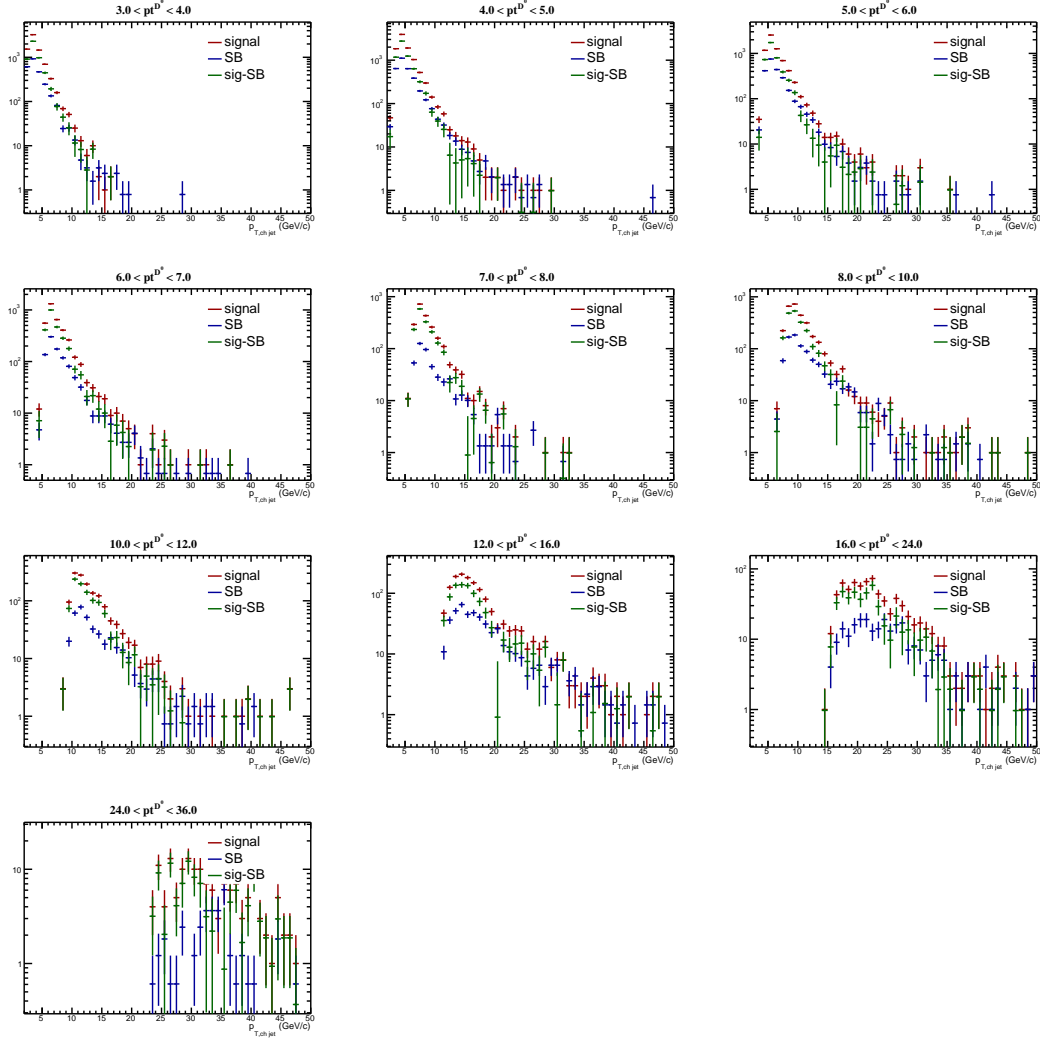


Fig. 10: Raw jet  $p_T$  distributions in bins of  $D^0$  transverse momentum in p-Pb collisions at  $\sqrt{s_{NN}} = 5.02$  TeV.

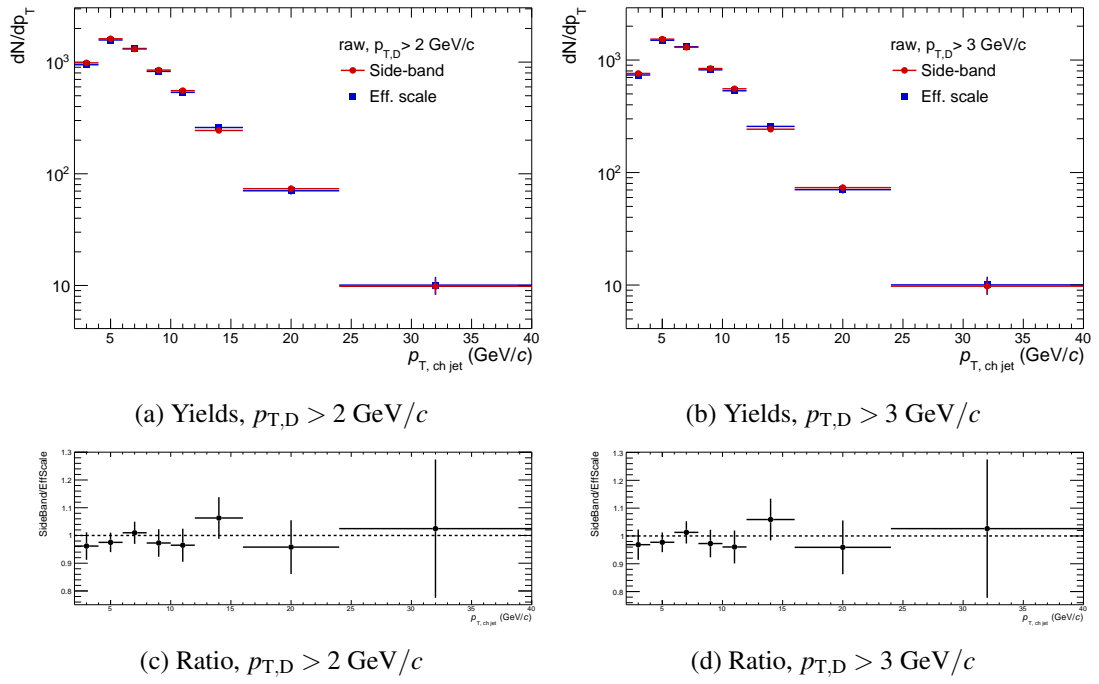


Fig. 11: Comparison of the raw yields obtained using the invariant mass fit method and the side band method without the efficiency correction for  $D^{*\pm}$ -jets in p-Pb collisions at  $\sqrt{s} = 5.02 \text{ TeV}$  with  $p_{T,D} > 2 \text{ GeV}/c$ (left) and  $p_{T,D} > 3 \text{ GeV}/c$ (right).

## 6 Efficiency Correction Procedure

### 6.1 Reconstruction Efficiency

The efficiency and acceptance ( $\text{Acc} \times \varepsilon$ ) were calculated using Monte Carlo PYTHIA6+GEANT3 simulations anchored to the data.

The efficiency is taken as the ratio of the  $p_{T,D}$  spectra of the D-tagged generator-level jets for which a matched D-tagged detector-level jet was found over all the generated D-tagged jets. For the detector-level jets, the D meson is required to be within the standard fiducial rapidity cuts. Jets are further requested to have  $|\eta_{\text{jet}}| < 0.9 - R$ , both at generator and detector levels.

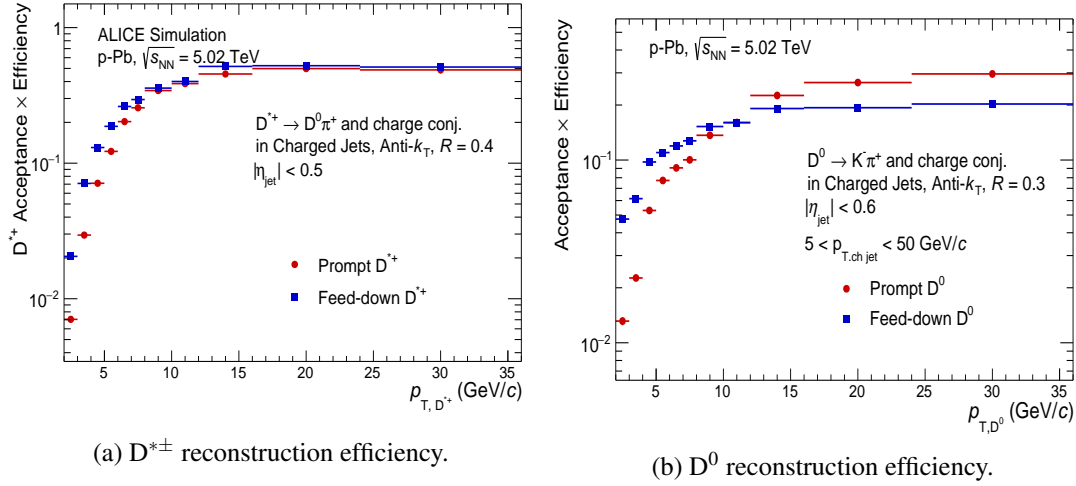


Fig. 12: D meson reconstruction efficiencies in p-Pb collisions at  $\sqrt{s_{\text{NN}}} = 5.02$  TeV, for prompt D mesons in red and non-prompt in blue.

Figures 12a and 12b show the  $D^{*\pm}$  and  $D^0$  reconstruction efficiencies as a function of  $p_{T,D}$  for prompt and non-prompt D-mesons. Efficiency depends strongly on  $p_{T,D}$  because of the topological cuts that are relaxed at higher momenta where the combinatorial background is smaller.

### 6.2 Efficiency-Corrected Yields

As discussed in the previous section, the D-meson reconstruction efficiency shows a strong dependence on  $p_{T,D}$  (but has very weak or no dependence on  $p_{T,\text{jet}}$ ). Therefore, in order to reduce the dependence on the Monte Carlo simulation for what concerns jet fragmentation and momentum spectral shape, the efficiency should be applied as a function of the D-meson momentum. In fact, each bin of  $p_{T,\text{jet}}$  has contributions from D mesons with very different  $p_{T,D}$ , which have different efficiencies.

The efficiency-rescaling procedure of the invariant mass distribution  $M(p_{T,\text{jet}}, p_{T,D})$  was implemented according to the following formula:

$$M(p_{T,\text{jet}}) = \sum_{p_{T,D}} \frac{M(p_{T,\text{jet}}, p_{T,D})}{(\text{Acc} \times \varepsilon)_{p_{T,D}}}. \quad (3)$$

Figures 13 and ?? show the  $D^{*\pm}$  and  $D^0$  invariant mass distributions for different ranges of  $p_{T,\text{chjet}}$ , after the efficiency reweighing procedure.

In the side-band method the efficiency correction is applied by rescaling the  $D^{*\pm}$  jet  $p_T$  spectra in Fig. 8 by  $1/(\text{Acc} \times \varepsilon)$  in each D-meson  $p_T$  bin shown in Fig. 12a. Likewise, the  $D^0$  jet  $p_T$  spectra in Fig. 10 are rescaled with  $D^0$   $p_T$  bin specific efficiencies in Fig. 12b. The background subtracted distributions are



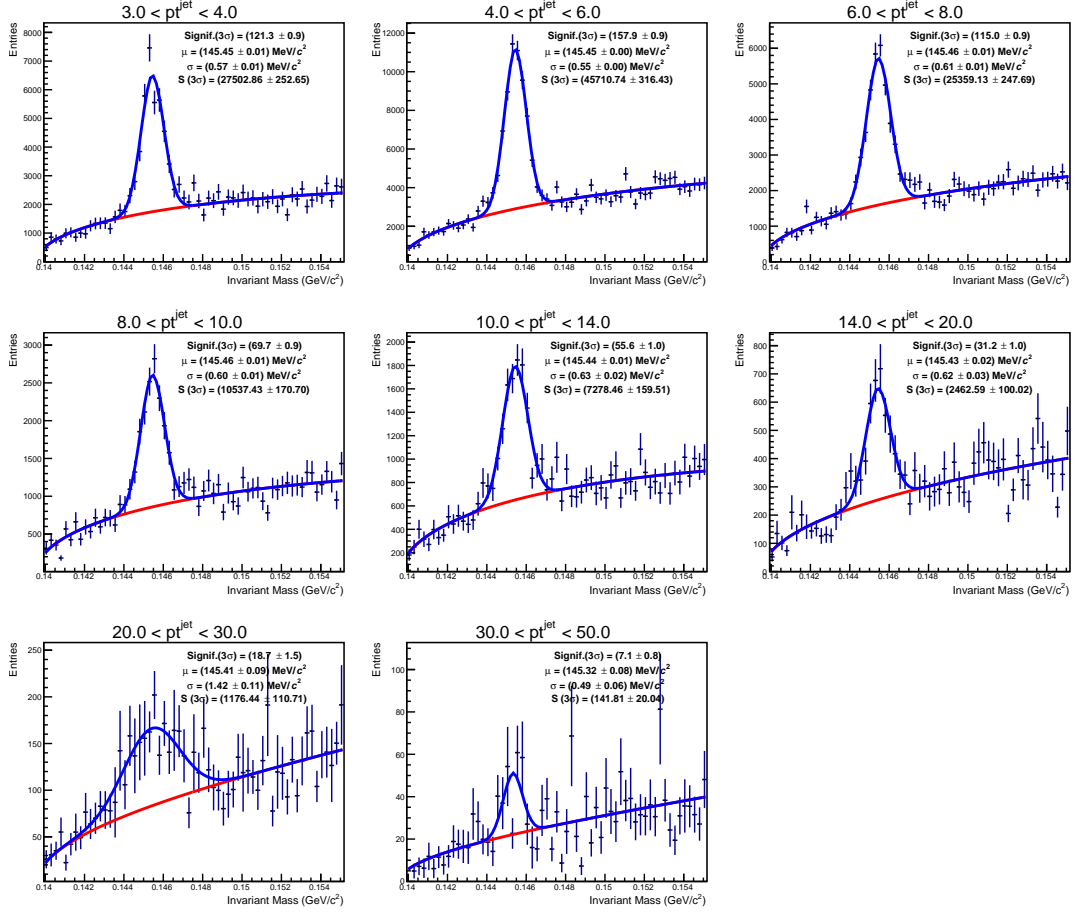


Fig. 13:  $D^{*\pm}$  signal extraction in bins of jet transverse momentum in p–Pb collisions at  $\sqrt{s_{NN}} = 5.02$  TeV. D mesons are required to have  $p_{T,D} > 3$  GeV/c. Each candidate is weighted by the inverse of the reconstruction efficiency, which depends on its  $p_{T,D}$ .

summed up to obtain the corrected jet  $p_T$  spectra for D-jets. The efficiency corrected jet  $p_T$  spectra are shown in Fig. 14 and Fig. 15 for  $D^{*\pm}$ -jets and  $D^0$ -jets respectively.

The efficiency corrected jet  $p_T$  spectra for both methods with the same binning are shown below.

### 6.3 Method Comparison (Efficiency-Corrected Yields)

Figure 16 and ?? show a comparison of the efficiency-corrected yields obtained using the direct jet- $p_T$  extraction method and the side band subtraction method for  $D^{*\pm}$ -jets and  $D^0$ -jets respectively with  $p_{T,D} > 2$  GeV/c and  $p_{T,D} > 3$  GeV/c. As mentioned before, the direct jet- $p_T$  extraction method is sensitive to weighing with low efficiency for low  $p_T$  D mesons. Therefore, discrepancies for higher  $p_{T,jet}$  ranges between two methods are visible with  $p_{T,D} > 2$  GeV/c cut. With  $p_{T,D} > 3$  GeV/c cut the two methods agree very well with each other within the statistical uncertainties.  $p_{T,D} > 3$  GeV/c cut reduces also uncertainties on the jet spectra for higher  $p_{T,jet}$ . Figures 17a and 17b show relative statistical uncertainties for the Side-Band subtraction method with  $p_{T,D} > 3$  GeV/c for  $D^{*\pm}$ -jets and  $D^0$ -jets.

The default method used for the further analysis is the Side Band method with  $p_{T,D} > 3$  GeV/c cut. The method is more stable, Gaussian fits perform better when they are done in  $p_{T,D}$  bins, and it is easier to perform the jet spectra analysis with more fine binning if needed.

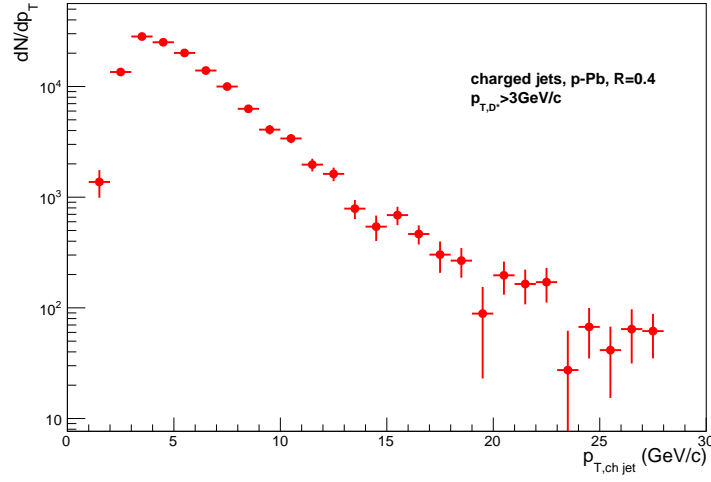


Fig. 14: Efficiency corrected  $D^{*\pm}$ -jets yield obtained for the Side-Band subtraction method in p-Pb collisions at  $\sqrt{s_{NN}} = 5.02$  TeV. D mesons are required to have  $p_{T,D} > 3$  GeV/c.

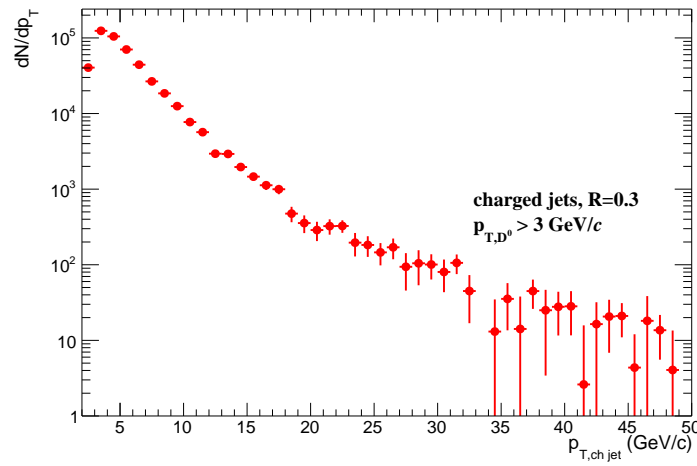


Fig. 15: Efficiency corrected  $D^0$ -jets yield obtained for the Side-Band subtraction method in p-Pb collisions at  $\sqrt{s_{NN}} = 5.02$  TeV. D mesons are required to have  $p_{T,D} > 3$  GeV/c.

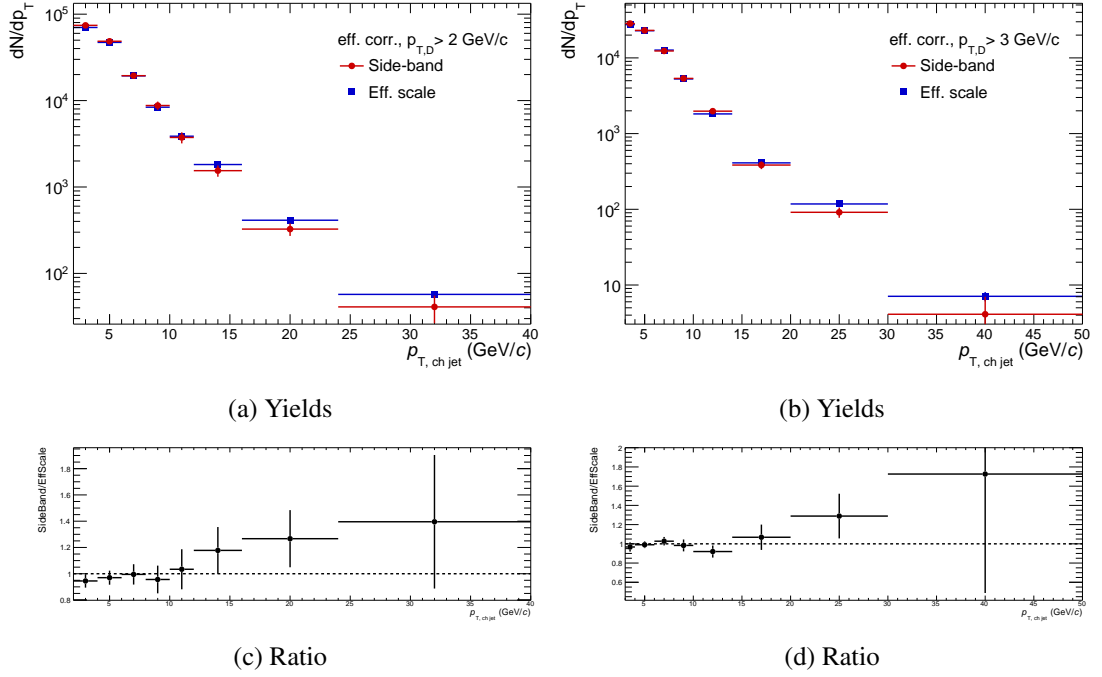


Fig. 16: Comparison of the yields obtained using the direct jet- $p_T$  extraction method and the side band subtraction method for  $D^{*\pm}$ -jets in p–Pb at  $\sqrt{s_{NN}} = 5.02$  TeV, with two cuts on  $p_{T,D}$ :  $p_{T,D} > 2$  GeV/ $c$  and  $p_{T,D} > 3$  GeV/ $c$ . Reconstruction efficiency correction is applied in both cases.

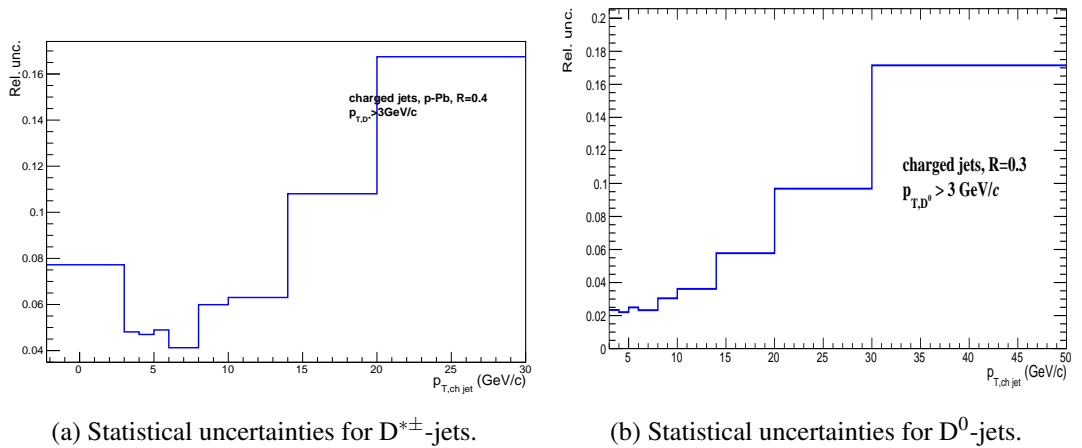


Fig. 17: Statistical uncertainties obtained using the side band method for  $D^{*\pm}$ -jets and  $D^0$ -jets in p–Pb at  $\sqrt{s_{NN}} = 5.02$  TeV, with  $p_{T,D} > 3$  GeV/ $c$ . Reconstruction efficiency correction is applied.

## 7 Underlying Event (p–Pb analysis)

### 7.1 Average Background Momentum Density

The Underlying Event (UE) affects the reconstructed jet momentum and needs to be subtracted. The average background density  $\rho$  is calculated on an event-by-event basis:

$$\rho_{\text{p-Pb}} = \text{median} \left\{ \frac{p_{\text{T,jet}}^{k_{\text{T}}}}{A_{\text{jet}}^{k_{\text{T}}}} \right\} C. \quad (4)$$

where  $p_{\text{T,jet}}^{k_{\text{T}}}$  and  $A_{\text{jet}}^{k_{\text{T}}}$  are respectively the transverse momentum and the area of the jets found using the  $k_{\text{T}}$  algorithm. The jet area is estimated by FASTJET using the active ghost method, with a ghost area of 0.005. The two leading jets in the event are excluded in order to remove the hard scattering jets from the background. This approach has been used extensively in jet reconstruction analyses [5, 6]. The corrected jet transverse momentum  $p_{\text{T,chjet}}^{\text{corr}}$  is obtained by subtracting the average background density times the jet area:

$$p_{\text{T,chjet}}^{\text{corr}} = p_{\text{T,chjet}}^{\text{raw}} - \rho A_{\text{jet}}. \quad (5)$$

For p–Pb collisions a procedure that takes into account sparse environment with the factor  $C$ , which is the occupancy correction factor, defined as:

$$C = \frac{\sum_j A_j}{A_{\text{acc}}}. \quad (6)$$

$A_j$  is the area of each  $k_{\text{T}}$  jet with at least one real track (i.e. excluding ghosts),  $A_{\text{acc}}$  is the area of charged-particle acceptance.

Figure 18 presents  $\rho$  distributions calculated in events that include D-jet candidates (the analysed events), and requiring that an event is with the leading jet that has  $p_{\text{T}} > 5 \text{ GeV}/c$ , for 0-10% (left) and 20-40% (right) centrality. The distributions are compared to  $\rho$  from events where a presence of D meson within a jet is not required (called inclusive-jet events).

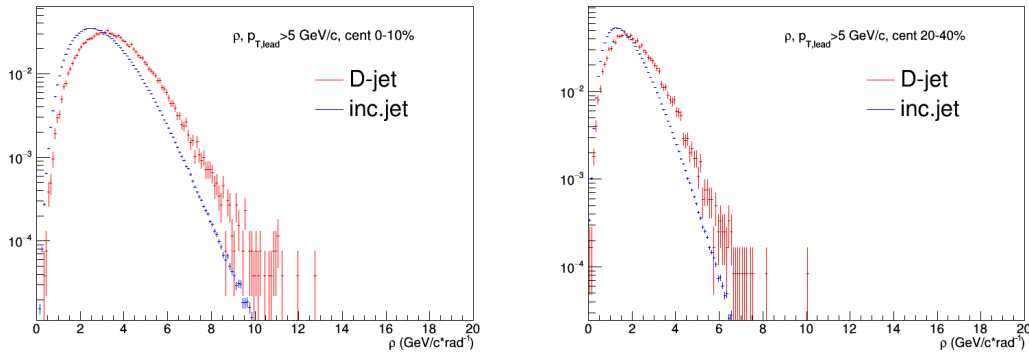


Fig. 18:  $\rho$  distributions from events with D-jet candidates, and with a leading jet that has  $p_{\text{T}} > 5 \text{ GeV}/c$ , for 0-10% (left) and 20-40% (right) centrality, compared to  $\rho$  from events from inclusive-jet events. p–Pb events with  $R = 0.4$ .

### 7.2 Jet Background Fluctuations

The amount of the jet background fluctuation was evaluated using the Random Cone method. This method consists in generating a random direction in  $\eta - \phi$  inside the jet detector acceptance and taking all tracks in the event that satisfy  $\Delta R < R_{\text{cone}}$  with  $R_{\text{cone}}$  equal to the resolution parameter used in the analysis. The raw cone  $p_{\text{T}}$  is the sum of the transverse momenta of all particles within the cone. The

background fluctuation  $\delta p_T$  is calculated as shown in Eq. 7, using events that include D-jet candidates excluding the leading jet in an event, and with the leading jet  $p_T > 5$  GeV/c. The distribution is shown in Fig. 19 as the left panel for  $D^{*\pm}$ -jets. Based on this distribution, a background fluctuation matrix is built which is then used to unfold the measured  $D^{*\pm}$ -jet  $p_T$  spectrum, together with the detector response matrix. The background fluctuation matrix for  $D^{*\pm}$ -jets is shown on the right panel of Fig. 19.

$$\delta p_T = p_{T,\text{cone}} - \rho \pi R_{\text{cone}}^2 \quad (7)$$

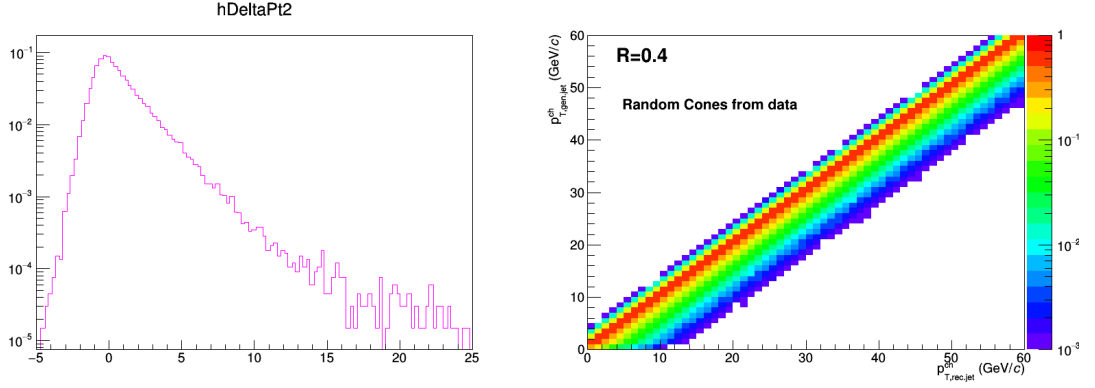


Fig. 19: Left:  $\delta p_T$  distribution obtained with Random Cone method. Right: The background fluctuation matrix built based on the  $\delta p_T$  distribution. p–Pb events with  $R = 0.4$ .

For  $D^0$ -jets, the background fluctuation  $\delta p_T$  is similarly calculated as for  $D^{*\pm}$ -jets using Eq. 7, but for  $R = 0.3$ , and the events used include D-jet candidates excluding the leading jet in an event. The leading jet is tagged with a D-meson candidate. Another case is considered where the random cone is especially placed in the perpendicular plane. In figure 20, on the left panel, a comparison is made between the  $\delta p_T$  distributions for these two cases and each case has excluded the D-tagged leading jet either having  $p_T > 5$  GeV/c or  $p_T > 10$  GeV/c. On the right panel shown is the background fluctuation matrix built using  $\delta p_T$  distribution for the excluded D-tagged leading jet with  $p_T > 5$  GeV/c and random cone thrown all over the  $\eta - \phi$  plane.

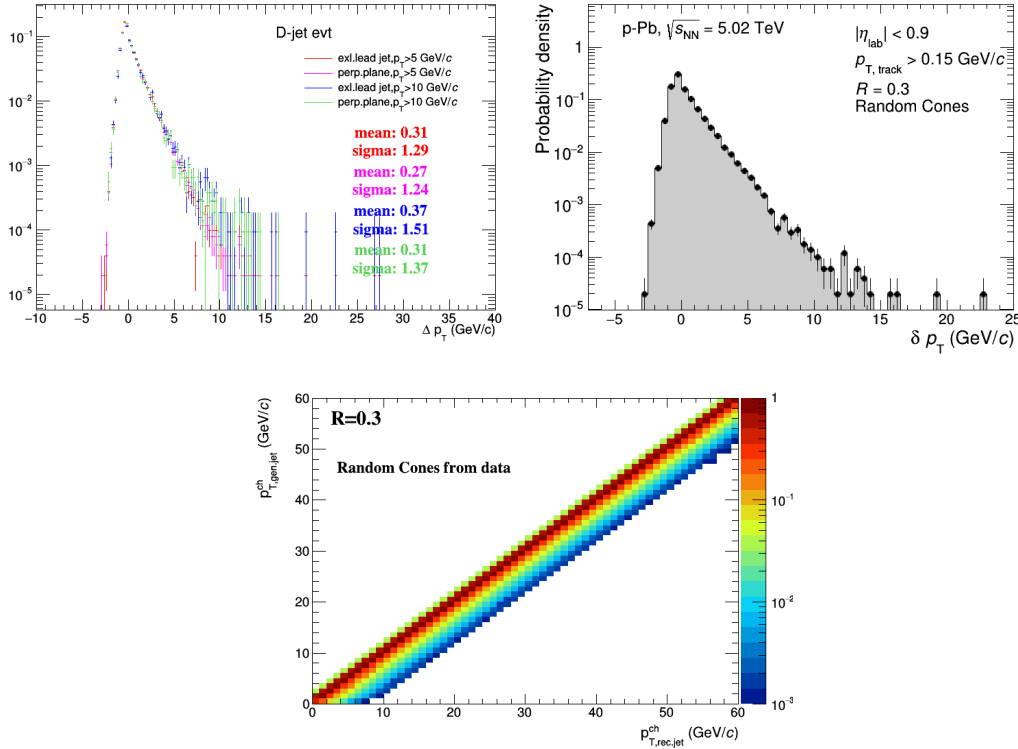


Fig. 20: Left:  $\delta p_T$  distributions from events with D-jet candidates, and with a D-tagged leading jet that has  $p_T > 5$  GeV/c, or  $p_T > 10$  GeV/c, random cone thrown randomly all over  $\eta - \phi$  or only in the perpendicular plane. Right:  $\delta p_T$  for excluded D-jet  $p_T > 5$  GeV/c, random cone not necessarily in the perpendicular plane. Bottom: The background fluctuation matrix built based on the  $\delta p_T$  distribution.

## 8 Jet Momentum Detector Response

The detector response is studied with a Monte Carlo simulation in which particles generated by an event generator are run through a transport code (GEANT3), that simulates the response of the detector elements, and then the same event reconstruction used in data is performed. Only  $c\bar{c}$  events are used.

Two sets of jets are obtained from the same event. One of them is obtained from the generator-level information and the second from the reconstructed signals after the detector simulation. The generated and reconstructed jets are matched by looking for the same D meson at both levels (using its MC label).

### 8.1 Detector Response Matrix

The detector response matrices for prompt and non-prompt  $D^{*\pm}$ -jets is shown in Fig. 21 and for  $D^0$ -jets in Fig. 22. The Monte Carlo production is with Hijing. However, in order to avoid Hijing imperfection of describing the underlying event, only the Pythia part of the production is used to extract the detector response matrix, and the background fluctuations matrix is obtained from data 7.2.

For both the  $D^{*\pm}$ -jets and  $D^0$ -jets, their respective prompt detector response matrices are used to unfold the measured D-jet  $p_T$  spectra after subtraction of the B feed-down component. For each D-jet, the B feed-down is estimated based on simulations, as described later, that is folded with the presented non-prompt detector response matrix combined with the background fluctuation matrix.

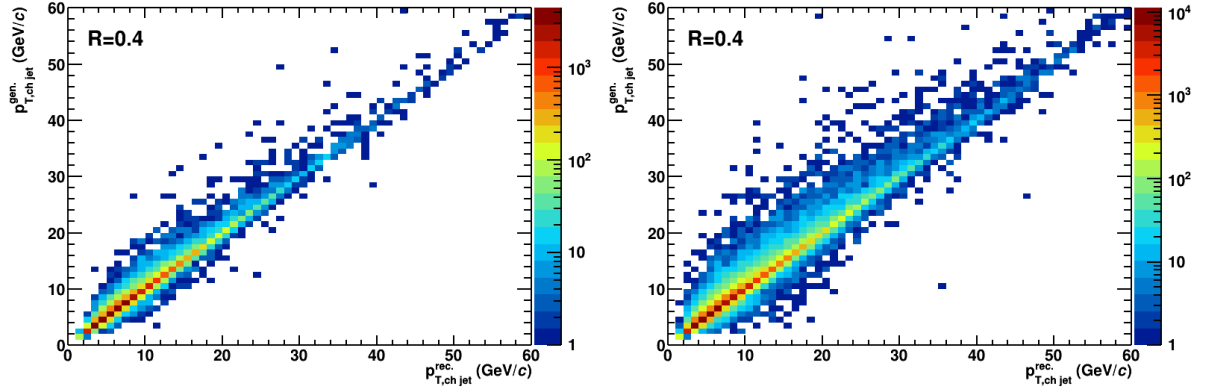


Fig. 21: Detector response matrix calculated with the PYTHIA part of the simulation of p–Pb events at  $\sqrt{s_{NN}} = 5.02$  TeV, for prompt (left) and non-prompt (right)  $D^{*\pm}$ -jet,  $R=0.4$ .

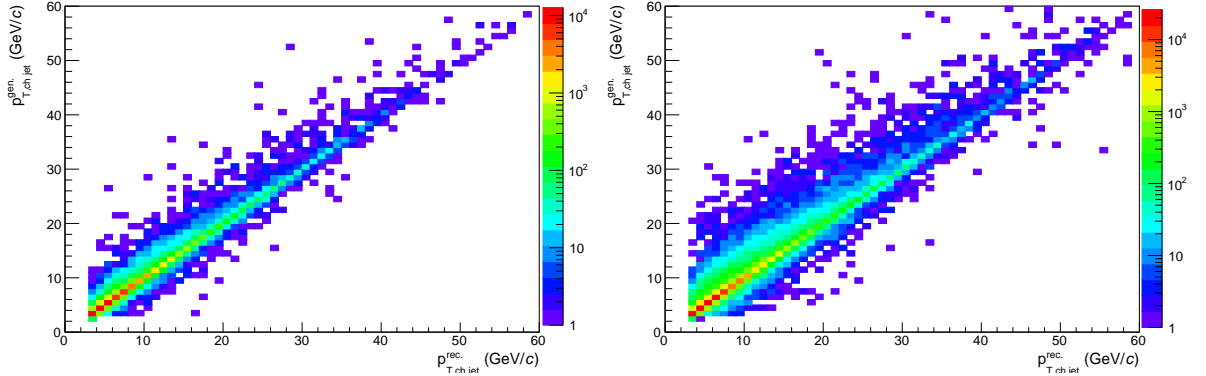


Fig. 22: Detector response matrix calculated with the PYTHIA part of the simulation of p–Pb events at  $\sqrt{s_{NN}} = 5.02$  TeV, for prompt (left) and non-prompt (right)  $D^0$ -jet,  $R=0.3$ .

## 9 Feed-Down Correction

A fraction of the measured D mesons originates from the decays of B mesons. These D mesons are usually referred to as non-prompt, to distinguish them from the prompt fraction, i.e. the ones that come directly from the fragmentation of a charm quark or decays of higher excited charm states. The longer decay length of B mesons combined with the topological cuts applied in the D meson selection causes the reconstruction efficiency to be higher for the non-prompt fraction compared to the prompt fraction. This is shown in Fig. 12a and 12b. As a consequence, the admixture of the prompt and non-prompt  $D - jets$  is biased in a detector-specific way towards the non-prompt. In order to make meaningful comparisons with theoretical and other experimental results one needs to either correct the bias or remove completely the non-prompt fraction and report only the prompt fraction. Both approaches require to use theoretical models or Monte Carlo simulations. In ALICE the second approach has been preferred so far, and for this analysis we decided to follow it.

### 9.1 Monte Carlo Simulation

For the D-meson spectra analysis, ALICE has used FONLL [7] calculations to estimate the non-prompt fraction [8, 9, 10]. In this analysis however we need to extract the B feed-down fraction also as a function of the jet kinematics, therefore this approach is not applicable. We decided to use POWHEG [11], a Monte Carlo event generator known to reasonably reproduce FONLL calculations and previous experimental results [12]. The second part of the parton shower and the fragmentation into hadrons is provided

by PYTHIA6 (Perugia-2011 tune). In addition a boost was applied in order to account for an asymmetric p–Pb collision system.

We generated 25 M  $c\bar{c}$  events and 25 M  $b\bar{b}$  events for the baseline parameters:  $m_c = 1.5 \text{ GeV}/c^2$ ,  $m_b = 4.75 \text{ GeV}/c^2$ ,  $\mu_R = \mu_F = \mu_0 = \sqrt{m^2 + p_T^2}$ , where  $m_c$  and  $m_b$  are receptively the charm and beauty masses,  $\mu_R$  and  $\mu_F$  are respectively the renormalization and factorization scale factors. Used based PDF set is: CT10NLO and nPDF: EPS09NLO.

The reconstruction of D-meson jets is performed in the POWHEG+PYTHIA events using the same procedure used for the main data analysis.

## 9.2 Feed-Down Subtraction

The B feed-down (FD) is subtracted from the measured D-meson jet  $p_T$  spectra by scaling the cross-section of D-meson jets obtained from the analysis of the POWHEG+PYTHIA simulation by the integrated luminosity of the analyzed data, according to Eq. 8:

$$N^{c \rightarrow D^{*\pm}}(p_{T,\text{chjet}}^{\text{det}}) = N^{c,b \rightarrow D^{*\pm}}(p_{T,\text{chjet}}^{\text{det}}) - R_{\text{det}}^{b \rightarrow D^{*\pm}}(p_{T,\text{chjet}}^{\text{det}}, p_{T,\text{chjet}}^{\text{part}}) \otimes \sum_{p_{T,D}} \frac{\epsilon^{b \rightarrow D^{*\pm}}(p_{T,D})}{\epsilon^{c \rightarrow D^{*\pm}}(p_{T,D})} N_{\text{POWHEG}}^{b \rightarrow D^{*\pm}}(p_{T,D}, p_{T,\text{chjet}}^{\text{part}}), \quad (8)$$

where:

- $N^{c \rightarrow D^{*\pm}}(p_{T,\text{chjet}}^{\text{det}})$  is the efficiency-corrected measured yield after FD subtraction;
- $N^{c,b \rightarrow D^{*\pm}}(p_{T,\text{chjet}}^{\text{det}})$  is the efficiency-corrected measured yield before FD subtraction;
- $R_{\text{det}}^{b \rightarrow D^{*\pm}}(p_{T,\text{chjet}}^{\text{det}}, p_{T,\text{chjet}}^{\text{part}})$  is the detector response matrix of the  $p_T$  of non-prompt  $D^{*\pm}$ -jets;
- the symbol  $\otimes$  is to be interpreted as the standard product of the response matrix times the vector of the yields in bins of  $p_{T,\text{chjet}}^{\text{part}}$ ;
- $\epsilon^{c \rightarrow D^{*\pm}}(p_{T,D})$  and  $\epsilon^{b \rightarrow D^{*\pm}}(p_{T,D})$  are respectively the reconstruction efficiencies of prompt and non-prompt  $D^{*\pm}$  mesons;
- $N_{\text{POWHEG}}^{b \rightarrow D^{*\pm}}(p_{T,D}, p_{T,\text{chjet}}^{\text{part}})$  is the cross-section of  $D^{*\pm}$ -jets from the POWHEG simulation scaled by the integrated luminosity of the analyzed data.

The POWHEG  $D^{*\pm}$ -jet spectrum is weighted with the ratio of the prompt over non-prompt efficiency because it is subtracted from the measured yield.

There are differences between the prompt and non-prompt response, for this reason the FD has to be subtracted before unfolding the measured spectrum; furthermore, as illustrated in Eq. 8, the spectrum obtained from the POWHEG simulation is smeared using the response of non-prompt  $D^{*\pm}$ -jets. Combined response matrix used to fold the simulated non-prompt spectrum is shown in Fig 23. Figure 24 compares the measured  $D^{*\pm}$ -jet  $p_T$  spectrum with the FD spectrum and the subtracted spectrum. Similar procedure is also employed for  $D^0$ -jets. Figure 25 compares the measured  $D^0$ -jet  $p_T$  spectrum with the FD spectrum and the subtracted spectrum.



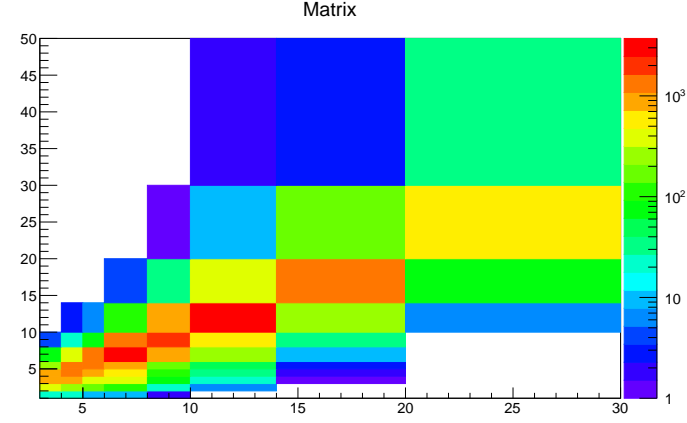


Fig. 23: Combined response matrix calculated with a full simulation of p-Pb events at  $\sqrt{s_{NN}} = 5.02$  TeV, for  $D^{*\pm}$ -jet.

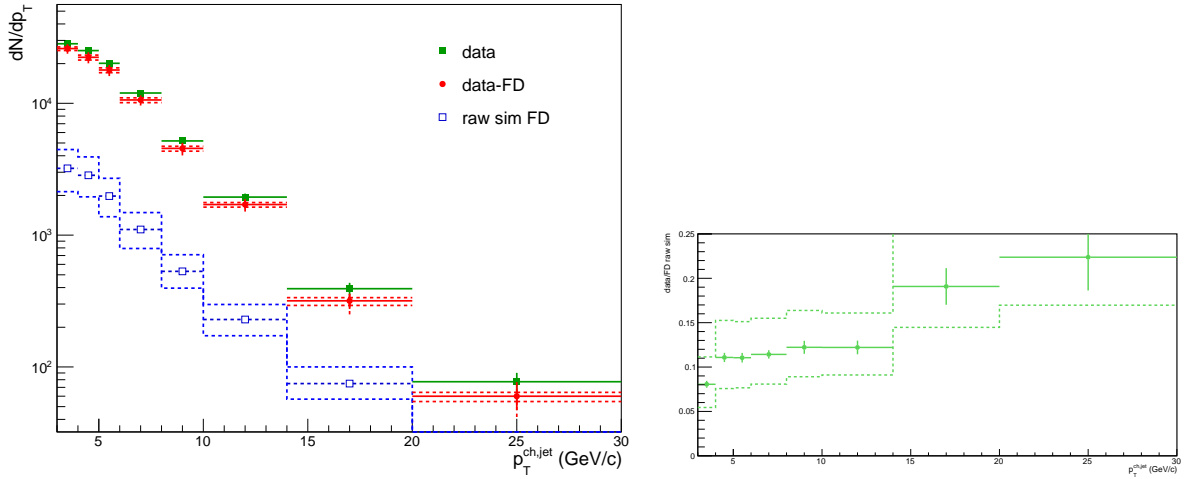


Fig. 24: Left: Efficiency-corrected measured  $D^{*\pm}$ -jet spectrum in p-Pb collisions at  $\sqrt{s_{NN}} = 5.02$  TeV before FD correction (green) and after FD correction (red). The FD spectrum is also plotted (blue) with its uncertainties. Right plot shows ratio of non-prompt to inclusive  $D^{*\pm}$ -jet spectrum.

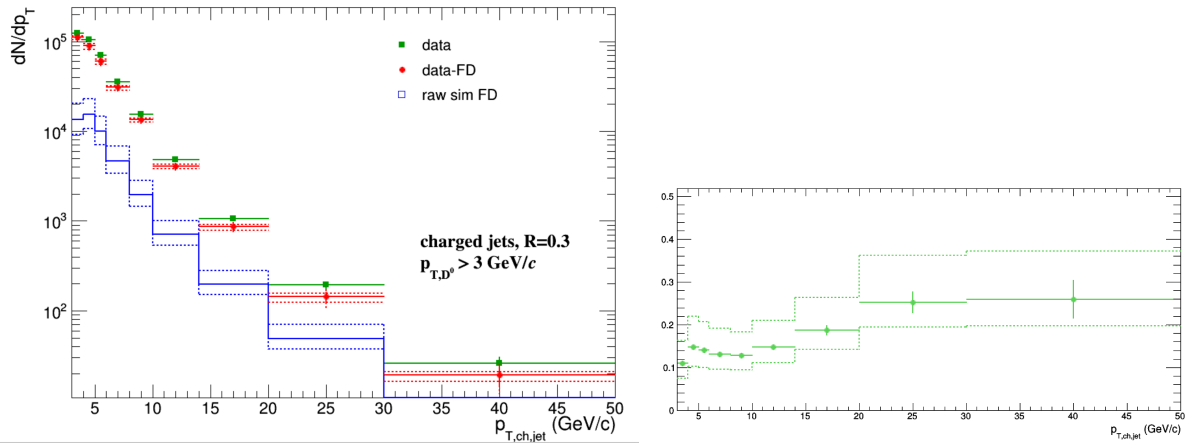


Fig. 25: Left: Efficiency-corrected measured  $D^0$ -jet spectrum in p-Pb collisions at  $\sqrt{s_{NN}} = 5.02$  TeV before FD correction (green) and after FD correction (red). The FD spectrum is also plotted (blue) with its uncertainties. Right plot shows ratio of non-prompt to inclusive  $D^0$ -jet spectrum.

## 10 Unfolding

Due to detector finite momentum resolution and tracking inefficiency the jet  $p_T$  spectra measured as described in the previous sections are distorted. In addition, in p–Pb collisions, fluctuations in the background momentum density introduce additional distortions. These distortions are detector-specific and do not allow a direct comparison with theoretical models and other independent experimental results.

In order to correct for these distortions, we first need to assess the detector performance and quantify the detector response to the D-meson jets. In addition, for the p–Pb analysis the background fluctuations are quantified in a fully data-driven fashion.

Figure ?? shows a combined response matrix in p–Pb used for the jet  $p_T$  spectra unfolding. The matrix is rebinned according to the binning used for the final jet  $p_T$  spectra. Then, the unfolding matrix, a distribution used as a prior and the corrected jet  $p_T$  spectrum obtained from the data are passed to the unfolding algorithm. The algorithm returns an unfolded jet  $p_T$  spectrum. As a prior, the spectrum obtained from the Monte Carlo simulation at the generator level is used.

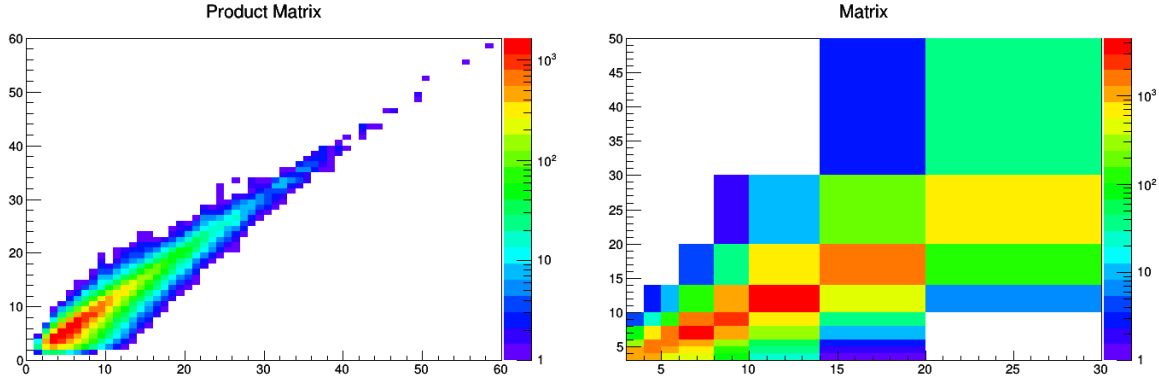


Fig. 26: Combined response matrix calculated with a full simulation of p–Pb events at  $\sqrt{s_{NN}} = 5.02$  TeV.

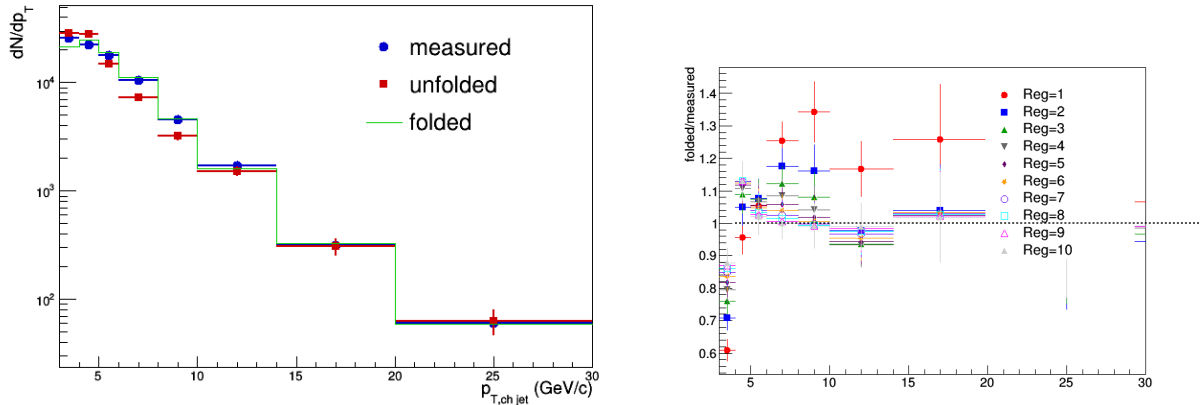


Fig. 27: Left: Corrected jet  $p_T$  spectrum before (blue) and after (red) the unfolding procedure (Bayesian method with five iterations), p–Pb events at  $\sqrt{s_{NN}} = 5.02$  TeV. Right: ratio to the measured spectrum to the folded for up to 10 iterations in the Bayesian unfolding, the considered jet  $p_T$  range is above 5 GeV/c.

Figure 27 presents corrected for the reconstruction efficiency and B feed-down jet  $p_T$  spectra before the unfolding (blue) and after the unfolding (red), for the side-band method. Unfolding is done with Bayesian and SVD (see 11.4) techniques using the RooUnfold software package. The default method is the Bayesian with five iterations. The green line represents folded back spectrum, and is compared to

the measured jet spectrum before unfolding with different iterations in the Bayes unfolding - right panel of Fig. 27, a considered in the analysis jet  $p_T$  range is above 5 GeV/ $c$ .

Comparison of unfolded spectra with different methods and priors is presented in the systematic uncertainties section.

## 11 Systematic Uncertainties

We considered the following sources of systematic uncertainties:

- Raw yield extraction
- D-Meson Selection Cuts
- B Feed-Down
- Unfolding and background fluctuation matrix
- Tracking Efficiency
- $p_T$  Shape of the Monte Carlo Spectrum

### 11.1 Raw Yield Extraction

The stability and systematics of the raw yield extraction has been assessed using the `MultiTrial` framework developed by the D2H group. This framework performs the fit of the invariant mass distribution many times varying several conditions, such as binning, fixed vs. free parameters, background function, fit range.

The following variations were included in the assessment of the systematics for the raw yield extraction of  $D^{*\pm}$  jets in p–Pb:

- fixed  $\sigma = \sigma_{MC}$ ;
- fixed  $\sigma = 1.15\sigma_{MC}$
- fixed  $\sigma = 0.85\sigma_{MC}$
- free  $\sigma$  and fixed  $m_0 = m_{PDG}$ ;
- fixed  $\sigma = \sigma_{MC}$  and  $m_0 = m_{PDG}$ ;
- free  $\sigma$  and free  $m_0$ ;
- background functions: power-law and power-law  $\times$  exponential;
- lower limit of fit range: 0.140, 0.142 GeV/ $c^2$ ;
- upper limit of fit range: 0.158, 0.160 GeV/ $c^2$ ;
- rebin by factor 2

Figure 28 shows the average of the yields obtained in each of these variations compared with the yields obtained with default fit settings as outlined in Section 5. The systematic uncertainties are calculated as the root-mean-square of all the yields obtained in the multi-trial fits and are shown in Fig. 29.

Figure 30 shows average of the multi-trial procedure for the side-band method as a function of jet  $p_T$  for each  $D^{*\pm}$   $p_T$  bin scaled by the corresponding efficiency, and average of the all  $D^{*\pm}$   $p_T$  bins (blue).

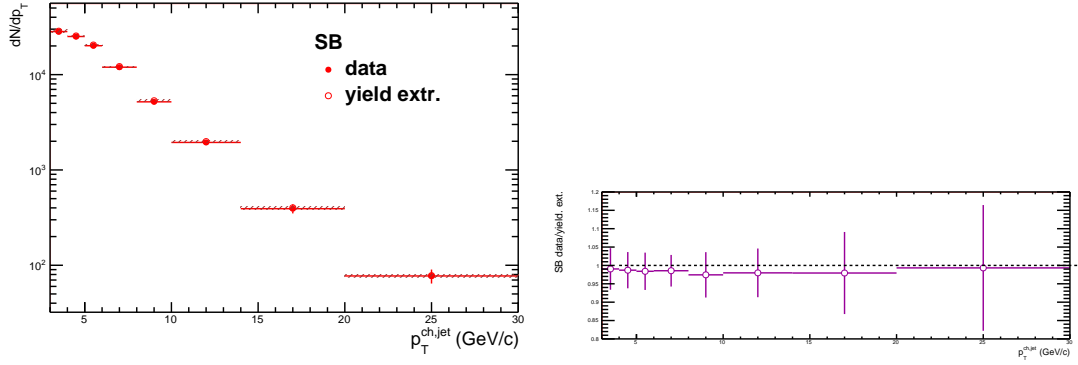


Fig. 28:  $D^{*\pm}$ -jet yields in p-Pb collisions obtained with the side-band method. On the left, the yields are shown with the default fit conditions (full markers) with error bars representing the statistical uncertainty and with the average of the multi-trial fit with filled rectangles representing the RMS of all the multi-trial yields; on the right a ratio of the central values obtained from the raw yield extraction procedure compared the yields obtained with default fit settings as outlined in Section 5.

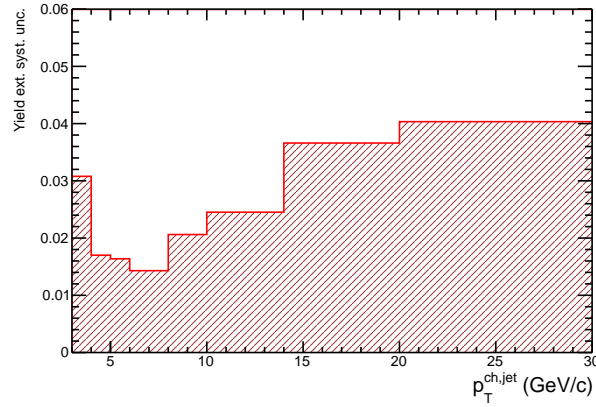


Fig. 29: The RMS of the multi-trial (systematic uncertainties).

## 11.2 D-Meson Selection Cuts

Uncertainties of the D-meson cut selection is estimated by varying applied in the analysis D-meson selection criteria, as reported in 3. Four variations are considered, two looser sets and two tighter sets of cuts with  $\pm 10\%$  and  $\pm 15\%$  variation from a default cut value. Raw  $D^{*\pm}$ -jet  $p_T$  distributions with these different cut sets and corresponding  $D^{*\pm}$ -jet efficiencies are shown in Fig. 31, and ratios in Fig. 32. Figure

Corrected for the corresponding efficiency  $D^{*\pm}$ -jet  $p_T$  distributions are presented in Fig. 34. Systematic uncertainties are estimated by taking ratio of the efficiency-corrected  $D^{*\pm}$ -jet  $p_T$  distributions with different cut variations to the  $D^{*\pm}$ -jet  $p_T$  spectrum obtained with the default cut set and taking RMS of them, as shown in Fig

## 11.3 B Feed-Down Correction

The B Feed-Down (FD) cross section is obtained from a POWHEG+PYTHIA6 simulation, as discussed in Section 9. In order to assess the systematic uncertainty the same simulation is performed with different

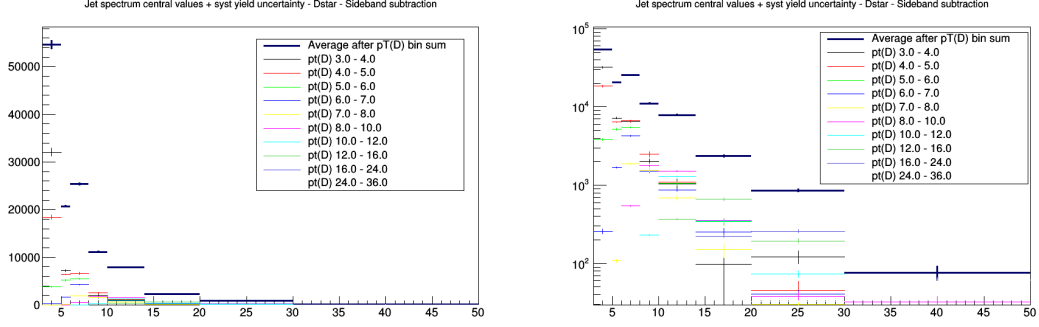


Fig. 30: Average of the multi-trial procedure for the side-band method as a function of jet  $p_T$  for each  $D^{*\pm}$   $p_T$  bin scaled by the corresponding efficiency, and average of the all  $D^{*\pm}$   $p_T$  bins (blue).

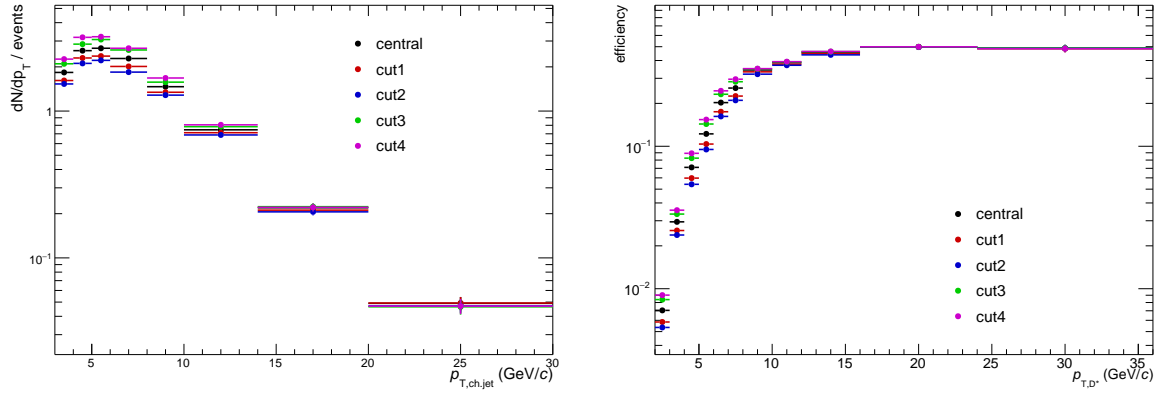


Fig. 31: Left:  $D^{*\pm}$ -jet  $p_T$  distributions with different cut sets for systematic uncertainties estimation. Right: corresponding  $D^{*\pm}$ -jet efficiencies.

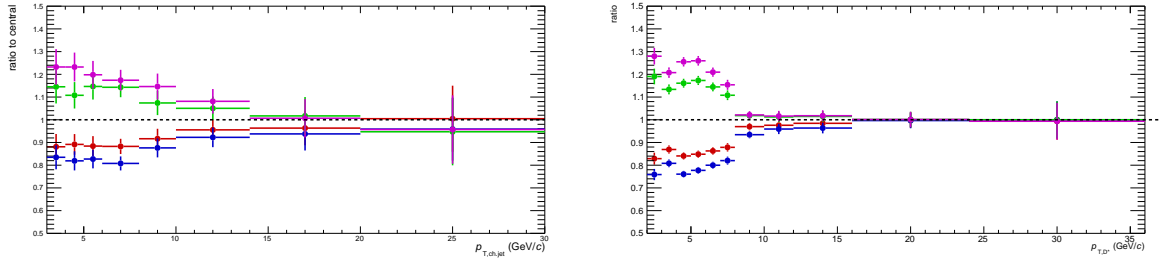


Fig. 32: Left: Ratios of  $D^{*\pm}$ -jet  $p_T$  distributions with different cut sets for systematic uncertainties estimation. Right: ratios of the corresponding  $D^{*\pm}$ -jet efficiencies.

choices of the quark mass  $m_b$ , the factorization scale factor  $\mu_F$ , and the renormalization scale factor  $\mu_R$ . Table 3 shows the list of parameters used to determine the central points and the variations used to determine the systematic uncertainty.

Figures 35 and 36 compare the cross sections obtained with the various choices of parameters listed in Table 3, respectively as a function of  $p_{T,D}$  and  $p_{T,chjet}$ . The  $p_{T,chjet}$  distribution is with the analysis cut on  $p_{T,D}$  3-36 GeV/c, and scaled by non-prompt to prompt efficiency ratio.

Figures 37 shows the final differential cross sections as a function of  $p_{T,chjet}$  with systematic uncertain-

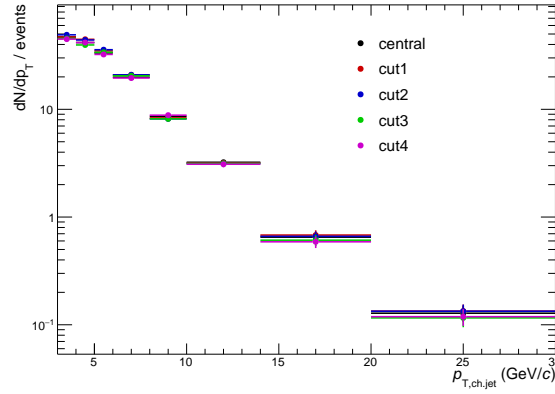


Fig. 33: Efficiency-corrected  $D^{*\pm}$ -jet  $p_T$  distributions with different cut sets for systematic uncertainties estimation.

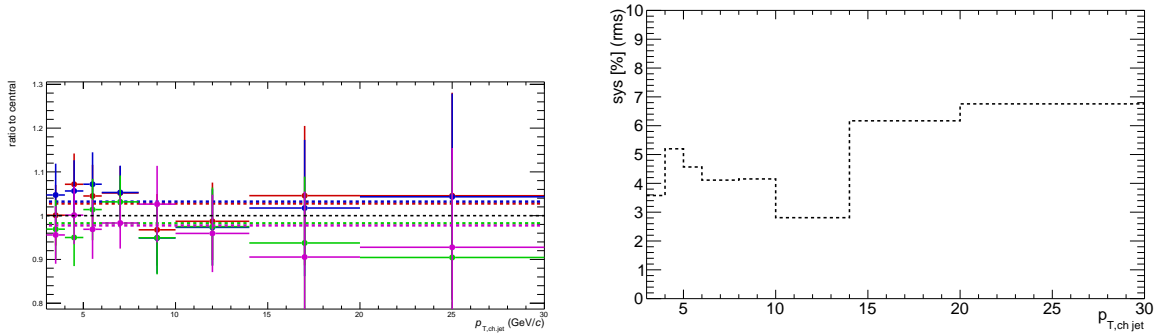


Fig. 34: Left: Ratio of the efficiency-corrected  $D^{*\pm}$ -jet  $p_T$  distributions with different cut sets for systematic uncertainties estimation. Right: RMS - systematic uncertainties.

Table 3: Parameters of the POWHEG+PYTHIA6 simulations used to estimate the B Feed-Down.

Parameter	Central Value	Variations
$m_b$	4.75 GeV/ $c^2$	4.5, 5.0 GeV/ $c^2$
PDF	CT10nlo (11000)	—
nPDF	EPS09nlo	—
$(\mu_F, \mu_R)$	(1,1)	(0.5,0.5), (0.5, 1), (1, 0.5), (2,2), (2,1), (1,2)

ties. The systematic uncertainties are obtained by taking the largest upward and downward variation from the central point in each bin. In this Figure uncertainties are therefore asymmetric. For the FD subtraction the largest between the upward and downward uncertainty is used in order to have a symmetric uncertainty.

#### 11.4 Unfolding

Figure 38 shows how the unfolded  $D^{*\pm}$ -jet spectrum in p-Pb collisions evolves with increasing number of iterations, and ratios of folded spectra with different iterations to the default iteration. Fig. 39 presents unfolded jet spectrum from the SVD method [13] on the left, and the right plot shows ratio of folded to measured spectra with different iterations. For the systematic uncertainty estimation also priors used for unfolding are varied. The baseline prior used for unfolding is the spectrum obtained (at generator level)

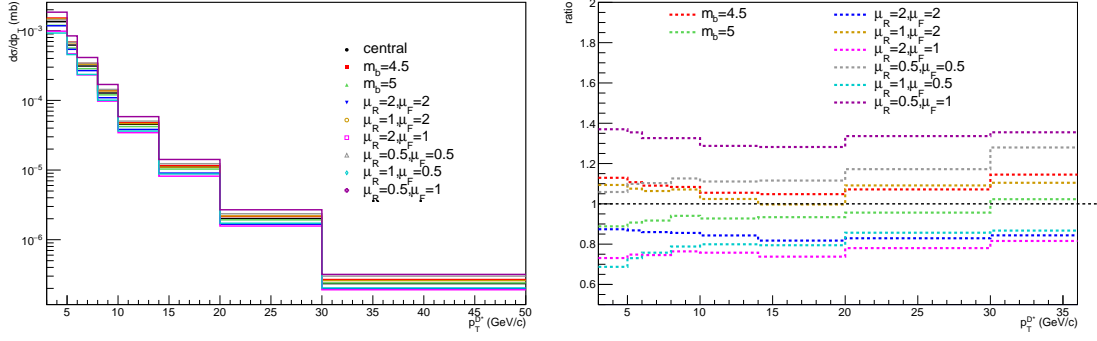


Fig. 35: Non-prompt (B Feed-Down)  $D^{*\pm}$ -jet cross section in p-Pb at  $\sqrt{s_{NN}} = 5.02$  TeV as a function of  $p_{T,D}$ , obtained in POWHEG+PYTHIA6 simulations with different choices of the simulation parameters.

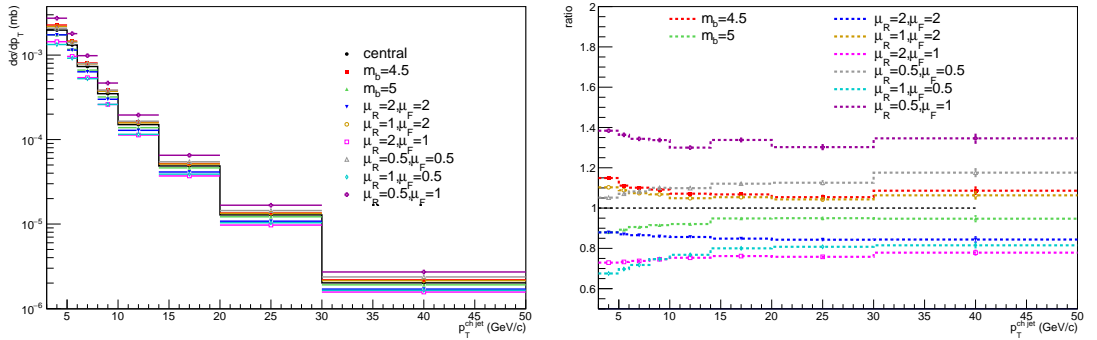


Fig. 36: Non-prompt (B Feed-Down)  $D^{*\pm}$ -jet cross section in p-Pb at  $\sqrt{s_{NN}} = 5.02$  TeV as a function of  $p_{T, \text{chjet}}$ , obtained in POWHEG+PYTHIA6 simulations with different choices of the simulation parameters,  $p_{T,D}$  3-36 GeV/c.

from PYTHIA. For the variations, the spectra were obtained from a modified power-law function:

$$f(p_{T,\text{jet}}) = p_{T,\text{jet}}^{-a} e^{-\frac{ab}{p_{T,\text{jet}}}}, \quad (9)$$

where  $a$  is the power-law index (we used two variations:  $a = 3, 6$ ) and  $b = 3$  GeV/c is the position of the local maximum of the distribution. The exponential factor  $e^{-\frac{ab}{p_{T,\text{jet}}}}$  was added to avoid infinities at zero and have a more realistic spectrum (the physical cross-section goes to zero for  $p_{T,\text{jet}} \rightarrow 0$ ).

Figure 40 compares the unfolded results obtained starting from three different priors in the Bayesian iterative method: PYTHIA spectrum, modified power-law with indexes 3 and 6 with 5 iterations, in the Bayesian iterative method with 8 iterations, and unfolded spectrum obtained using SVD with 5 iterations. Figure 41 presents ratio of these different unfolded spectra and RMS - systematic uncertainty.

### 11.5 Background fluctuation matrix

The background fluctuation matrix is determined in a data-driven way using the Random Cone method. The default background fluctuation  $\delta p_T$  is calculated using events that include D-jet candidates excluding the leading jet in an event, and with the leading jet  $p_T > 5$  GeV/c. For a systematic uncertainty estimation the  $\delta p_T$  is also calculated in inclusive-jet events, and with a requirement of the leading jet  $p_T > 10$  GeV/c for both D-jet candidate and inclusive-jet events. These different distributions are shown in Fig. 42 for events with the leading jet  $p_T > 5$  GeV/c (left) and 10 GeV/c (right). Based on these  $\delta p_T$  distributions, new background fluctuation matrices are build. They are then used to build a combined prompt response

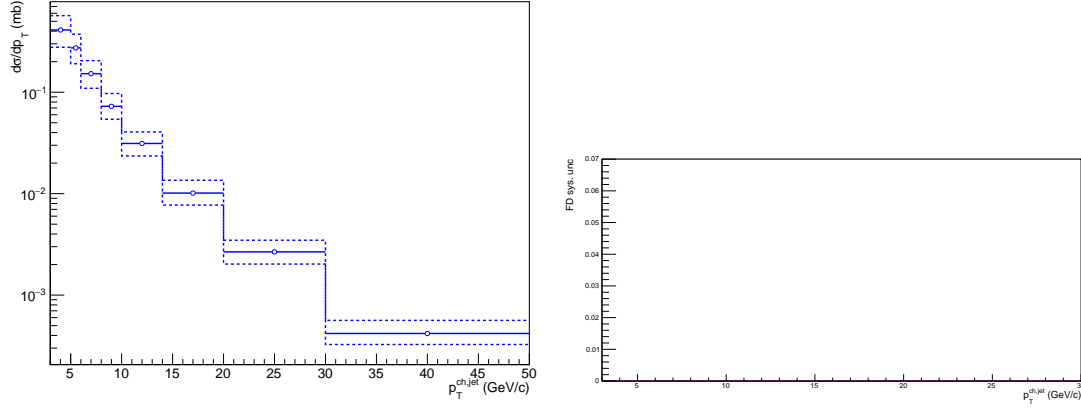


Fig. 37: Left: Non-prompt (B Feed-Down)  $D^{*\pm}$ -jet cross section in p-Pb at  $\sqrt{s_{\text{NN}}} = 5.02$  TeV, obtained in a POWHEG+PYTHIA6 simulation with the systematic uncertainty. Right: Final systematic uncertainties after the B feed-down subtraction from the inclusive  $D^{*\pm}$ -jet spectrum.

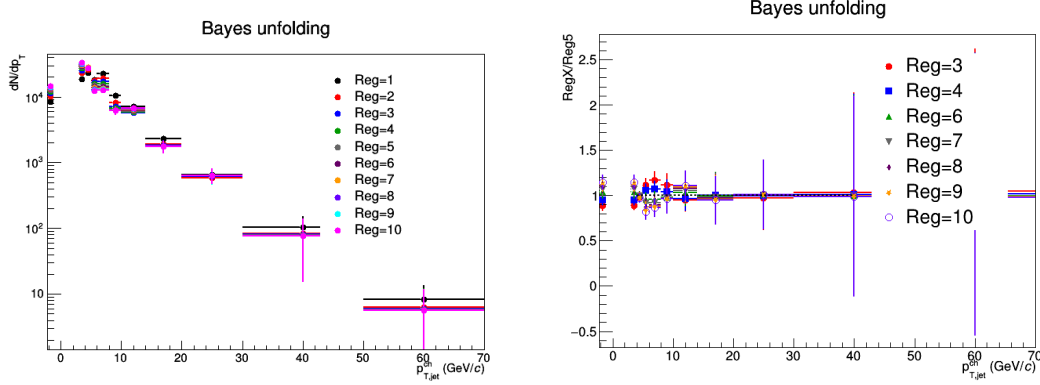


Fig. 38: The evolution of the unfolded spectra with increasing number of iterations for the Bayesian method is shown in different colors. The ratios between each number-of-iteration choices and the baseline (5 iterations) are shown on the right.

matrix and the measured  $D^{*\pm}$ -jet  $p_T$  spectrum is unfolded. Ratios of the unfolded spectra and RMS are shown in Fig. 44.

## 11.6 Tracking Efficiency

Uncertainties on the tracking efficiency affect the measurement in two ways.

First, it introduces an uncertainty on the D-meson reconstruction efficiency. This was evaluated for the D-meson spectra to be 4-4.5% (mostly  $p_T$ -independent). Since we have verified that the reconstruction efficiency itself does not depend on  $p_{T, \text{ch,jet}}$  we can assume that our measurement is affected by the same uncertainty.

Tracking efficiency also affects the detector response. To estimate the uncertainty on the final yield, a new detector response has been built where the efficiency has been reduced to 96% of its normal value, by throwing randomly away 4% of the reconstructed track in the simulation. The raw spectrum is unfolded using this modified response matrix and the outcome is compared with the reference result. The resulting systematic uncertainty is presented in Fig. 46. As a cross-check of the observed effect the efficiency was also reduced to 95%, the value used for the previous pp analysis - the found uncertainties agree between the two analysis.



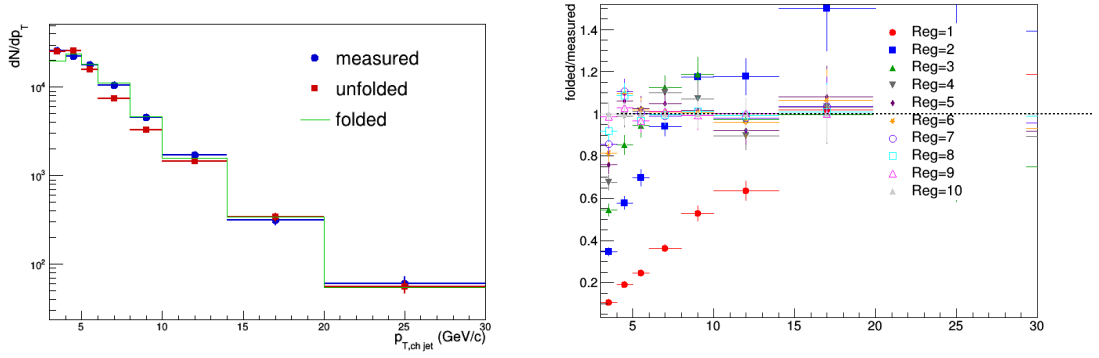


Fig. 39: The spectrum unfolded with the SVD method  $k = 5$  is shown on the left plot, and a comparison to the unfolded spectrum obtained using the Bayesian method is shown on the right. The ratios between folded and measured spectrum for each number-of-iteration choices are shown on the right.

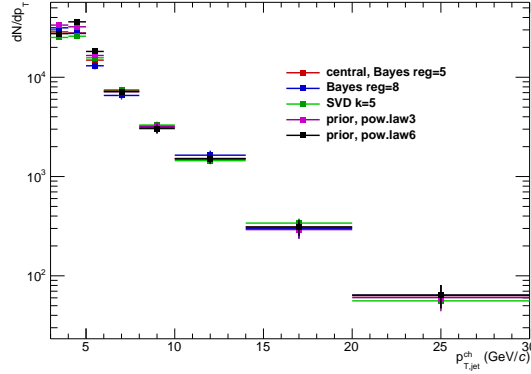


Fig. 40: Comparison of the unfolded results obtained starting from three different priors in the Bayesian iterative method: PYTHIA spectrum, modified power-law with indexes 3 and 6 with 5 iterations, in the Bayesian iterative method with 8 iterations, and unfolded spectrum obtained using SVD with 5 iterations.

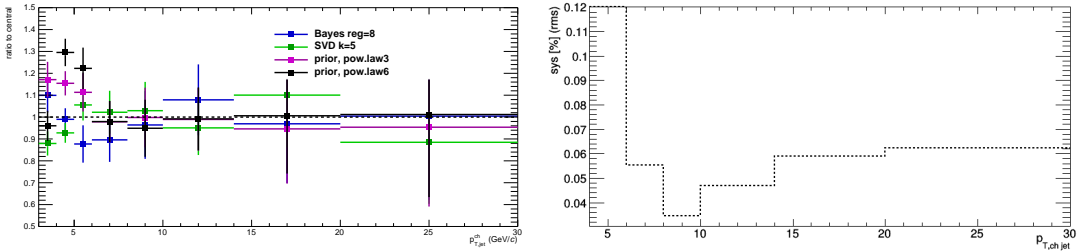


Fig. 41: Left: Ratio of the unfolded results obtained starting from three different priors in the Bayesian iterative method: PYTHIA spectrum, modified power-law with indexes 3 and 6 with 5 iterations, in the Bayesian iterative method with 8 iterations, and unfolded spectrum obtained using SVD with 5 iterations. Right: RMS – systematic uncertainty.

The systematic uncertainty is estimated by fitting the ratio and as the uncertainty the value obtained from the fitted function is used. The three cases, of 4, 5 and 10% inefficiency are fitted in order to check linearity, the quoted uncertainty is assumed to be symmetric.

### 11.7 $p_T$ Shape of the Monte Carlo Spectrum

The  $D^{*\pm}$  reconstruction efficiency is estimated using a PYTHIA6+GEANT3 simulation. A possible source of systematic uncertainty is the  $p_{T,D}$  shape of the Monte Carlo spectrum. Since the efficiency is

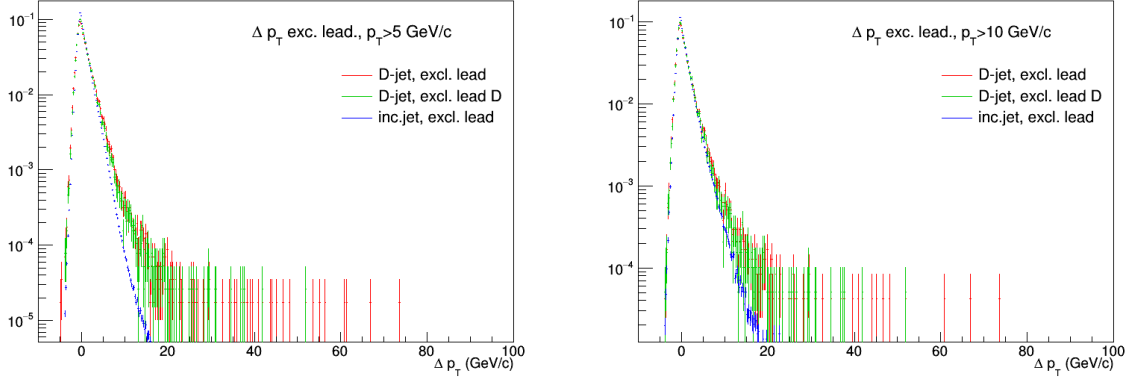


Fig. 42:  $\delta p_T$  distributions from D-jet candidate (red) and inclusive-jet (blue) events, and with a requirement of the leading jet  $p_T > 5$  GeV/c (left) and 10 GeV/c (right).

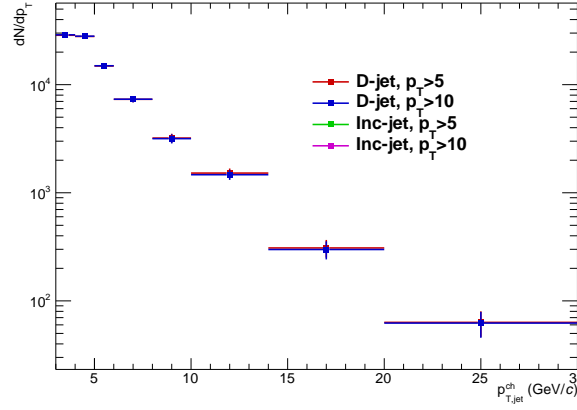


Fig. 43: Comparison of unfolded  $D^{*\pm}$ -jet  $p_T$  spectra with different background fluctuation matrices.

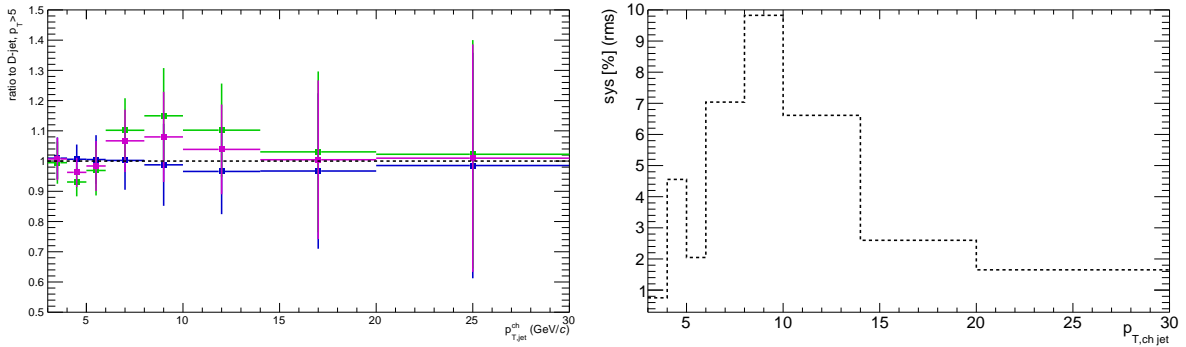


Fig. 44: Left: Ratio of unfolded  $D^{*\pm}$ -jet  $p_T$  spectra with different background fluctuation matrices. Right: RMS – systematic uncertainty.

calculated as a function of D meson , the shape of the D meson  $p_{T,D}$  spectrum is compared to FONLL, a parallel studies within the D2H group were performed. In this Monte Carlo production the generated shape and the FONLL shape agree with each other very well. Therefore, no systematic uncertainties from the  $p_{T,D}$  shape of the Monte Carlo Spectrum are assigned.

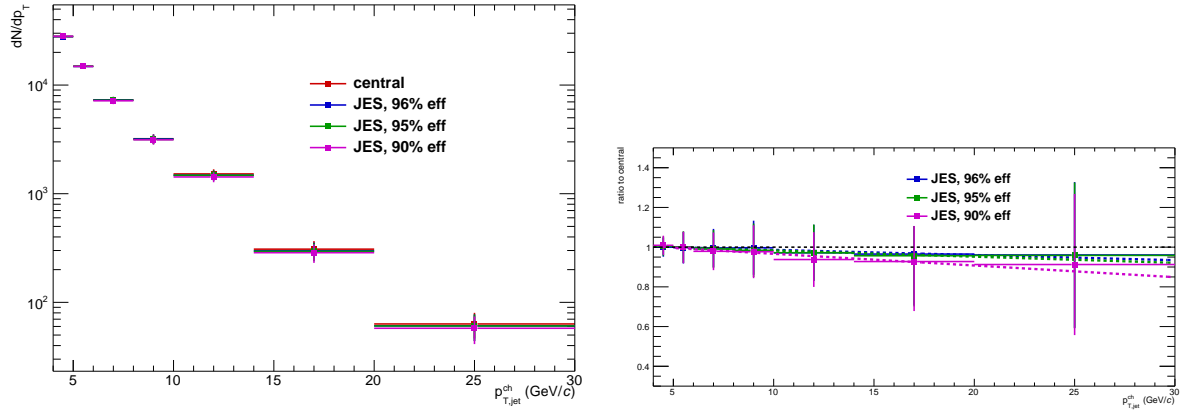


Fig. 45: Unfolded spectra (left) and a ratio (right) between default unfolding result and with reduced tracking efficiency to 96 and 95%.

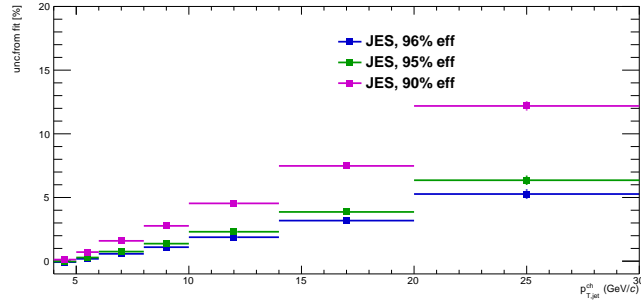


Fig. 46: Systematic uncertainty from the JES, for 4, 5 and 10% inefficiency. The final uncertainty is taken from the 96% efficiency case.

### 11.8 Summary of Systematic Uncertainties

The  $p_T$ -independent uncertainties are listed in Table 4. The summary of all uncertainties, including statistical uncertainties are listed for all  $p_{T, \text{chjet}}$  bins of the final spectrum in Table 5.

Table 4: Normalization systematic uncertainties.

Source	Uncertainty (%)
Branching Ratio	1.3
Luminosity	3.7
Total	3.9

Table 5: Summary of all uncertainties.

Source	Uncertainty (%)					
$p_{T, \text{chjet}} \text{ (GeV}/c\text{)}$	5 - 6	6 - 8	8 - 10	10 - 14	14 - 20	20 - 30
Raw Yield Extraction	2	2	2	3	4	4
Selection Cuts	5	4	4	4	6	7
B Feed-Down	5	5	5	5	8	9
Unfolding	12	6	4	5	6	6
Bkg. fluctuations	2	7	10	6	3	2
Tracking Eff. (D-Meson)	4	4	4	4	4	4
Tracking Eff. (Jet Energy Scale)	0	1	1	2	3	5
Total Systematic Uncertainty	15	12	13	11	14	15
Normalization Uncertainty	3.9					
Statistical	5.6	6.8	9.7	10.2	18.6	26.6

## 12 Results

This Section contains a summary of the results. The  $D^{*+}$ -jet  $p_T$ -differential cross-section in p-Pb collisions at  $\sqrt{s_{NN}} = 5.02$  TeV with all corrections applied (reconstruction efficiency, B feed-down subtraction, unfolding for detector momentum resolution); The cross-section is calculated according to the following formula:

$$\frac{d^2\sigma}{d\eta dp_T} = \frac{1}{L_{\text{int}} f_{\text{BR}}} \frac{N_{\text{D-jets}}(p_{T,\text{jet}})}{\Delta p_{T,\text{jet}} \Delta \eta}, \quad (10)$$

where  $L_{\text{int}} = N_{\text{evt}}/\sigma_{\text{inel}}$  is the integrated luminosity ( $\sigma_{\text{pPb,inel}} = 2.09$  b),  $f_{\text{BR}}$  is the branching ratio of the D-meson decay channel used in the analysis,  $N_{\text{D-jets}}(p_{T,\text{jet}})$  is the measured number of D-jets in a given  $p_{T,\text{jet}}$  bin (with all corrections applied).

The  $D^{*+}$ -tagged jet  $p_T$  differential cross section in p-Pb collisions at  $\sqrt{s_{NN}} = 5.02$  TeV is shown in Fig 47.

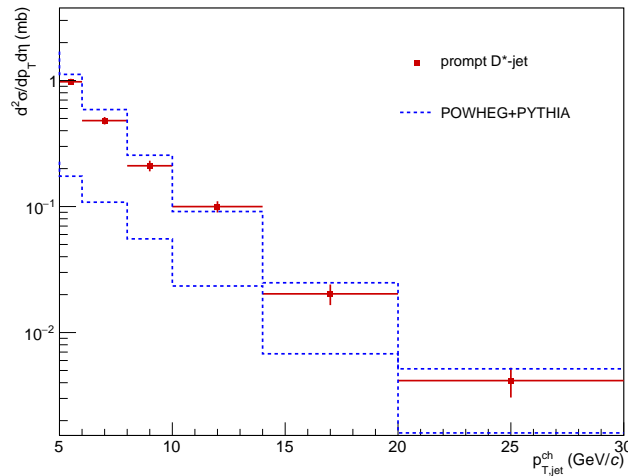


Fig. 47: Unfolded  $D^{*\pm}$ -jet spectrum in p-Pb collisions at  $\sqrt{s_{NN}} = 5.02$  TeV compared to PYTHIA+POWHEG simulations, with the simulation uncertainty.

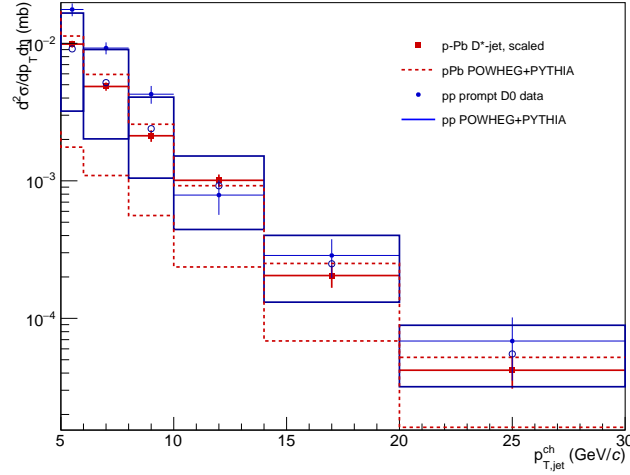


Fig. 48:  $D^{*+}$ -jet spectrum in p–Pb collisions at  $\sqrt{s_{NN}} = 5.02$  TeV compared  $D^0$ -jet spectrum in pp collisions at  $\sqrt{s} = 72$  TeV and PYTHIA+POWHEG simulations for pp.

### 12.1 Monte Carlo Simulations

We performed a set of Monte Carlo simulations using POWHEG and PYTHIA6 to compare with our measurement. The simulations follow the same recipe used for simulating the non-prompt fraction for the B feed-down correction. We simulated 25 M  $c\bar{c}$  events with POWHEG+PYTHIA6 for the central points plus several variations of the parameters of the simulation, listed in Table 6.

Table 6: Parameters of the POWHEG+PYTHIA6 simulations of  $c\bar{c}$  events used to compare with our measurement.

Parameter	Central Value	Variations
$m_b$	1.5 GeV/ $c^2$	1.3, 1.7 GeV/ $c^2$
PDF	CT10nlo (11000)	—
nPDF	EPS09nlo	—
$(\mu_F, \mu_R)$	(1,1)	(0.5,0.5), (0.5, 1), (1, 0.5), (2,2), (2,1), (1,2)

Figures 49 and 50 compare the cross sections obtained with the various choices of parameters listed in Table 6, respectively as a function of  $p_{T,D}$  and  $p_{T, \text{chjet}}$ .

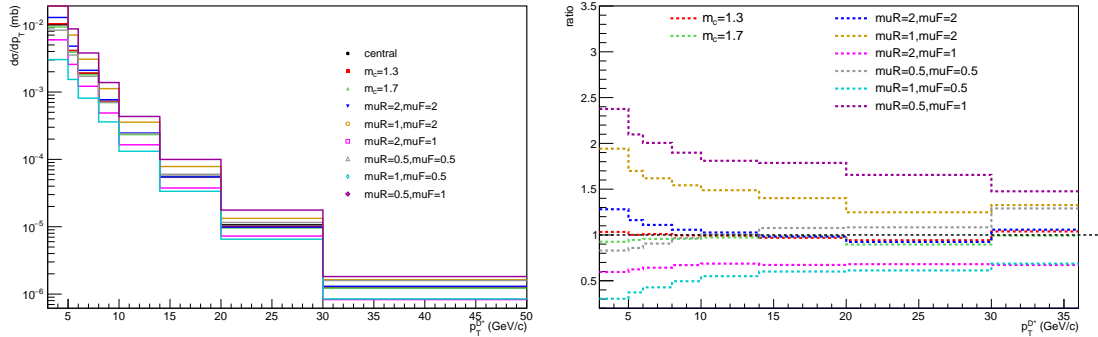


Fig. 49: Prompt  $D^{*\pm}$ -jet cross section in p–Pb at  $\sqrt{s_{NN}} = 5.02$  TeV as a function of  $p_{T,D}$ , obtained in POWHEG+PYTHIA6 simulations with different choices of the simulation parameters.

The systematic uncertainties are obtained by taking the largest upward and downward variation.

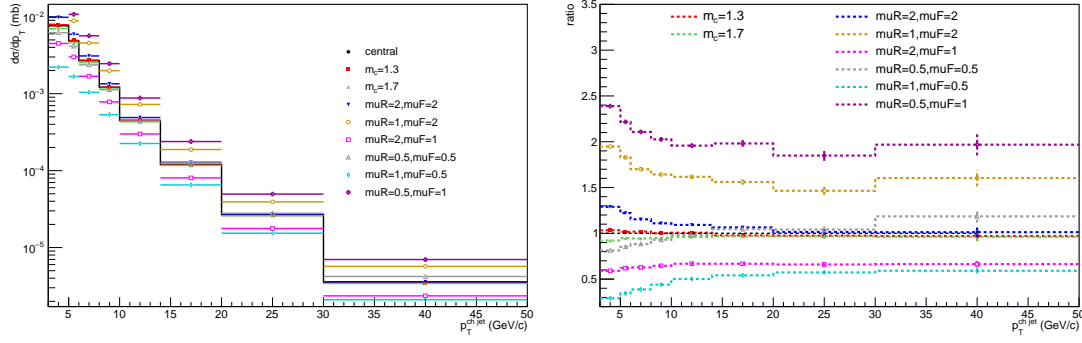


Fig. 50: Prompt  $D^{*\pm}$ -jet cross section in p-Pb at  $\sqrt{s_{NN}} = 5.02$  TeV as a function of  $p_{T, \text{chet}}$ , obtained in POWHEG+PYTHIA6 simulations with different choices of the simulation parameters, and the analysis cut of  $p_{T,D}$  3-36 GeV/c.

### 12.1.1 Effect of the $p_{T,D}$ Cut

The effect of the  $p_{T,D}$  cut in the  $D^{*\pm}$ -jet differential cross section has been studied in POWHEG+PYTHIA6. Figure 51 shows that the ratio of the cross section for  $p_{T,D} > 3$  GeV/c over inclusive is about 80% for  $p_{T, \text{chet}} = 4$  GeV/c and then it raises and reaches a plateau at about 95% for  $p_{T, \text{chet}} = 10$  GeV/c.

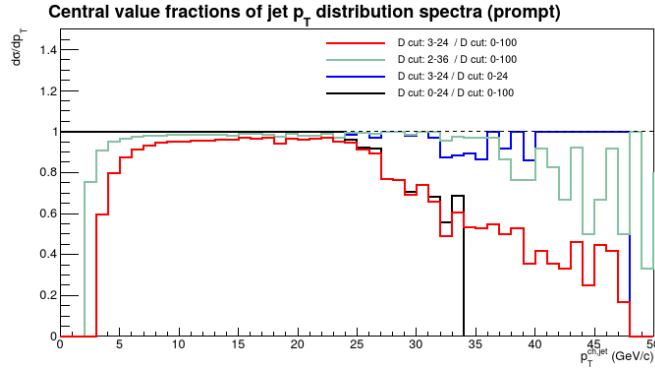


Fig. 51: Prompt  $D^{*\pm}$ -jet cross section in p-Pb at  $\sqrt{s_{NN}} = 5.02$  TeV as a function of  $p_{T, \text{chet}}$ , obtained in POWHEG+PYTHIA6 simulations, with no  $p_{T,D}$  cut as default, with  $2 < p_{T,D} < 36$  (green) and  $4 < p_{T,D} < 24$  GeV/c (red).

## 13 Preliminary Figures

Preliminary figure: Prompt  $D^{*+}$ -jet cross section in p-Pb at  $\sqrt{s_{NN}} = 5.02$  TeV as a function of  $p_{T, \text{chet}}$ , compared to POWHEG+PYTHIA6 simulations.

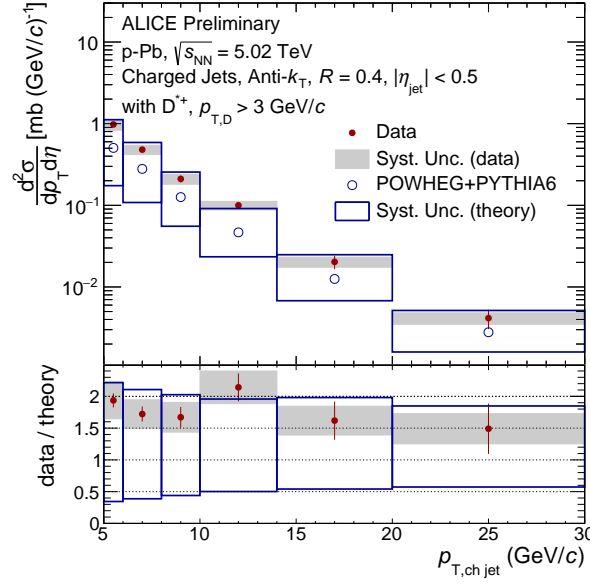


Fig. 52: Prompt  $D^{*+}$ -jet cross section in p–Pb collisions at  $\sqrt{s_{NN}} = 5.02$  TeV compared to POWHEG+PYTHIA6 simulations for p–Pb collisions at  $\sqrt{s_{NN}} = 5.02$  TeV.

## References

- [1] Patrignani C *et al.* (Particle Data Group) 2016 *Chin. Phys. C* **40** 100001
- [2] Cacciari M, Salam G P and Soyez G 2012 *Eur.Phys.J.* **C72** 1896 (*Preprint* 1111.6097)
- [3] Cacciari M, Salam G and Soyez G 2008 *JHEP* **04** 063
- [4] Cacciari M and Salam G 2006 *Physics Letters B* **641** 57–61
- [5] Abelev B *et al.* (ALICE) 2014 *JHEP* **1403** 013 (*Preprint* 1311.0633)
- [6] Adam J *et al.* (ALICE) 2015 *Phys. Lett. B* **746** 1 – 14 ISSN 0370-2693 (*Preprint* 1502.01689)
- [7] Cacciari M, Greco M and Nason P 1998 *JHEP* **9805** 007 (*Preprint* 9803400)
- [8] Abelev B *et al.* (ALICE) 2012 *JHEP* **2012** 1–30 ISSN 1029-8479 (*Preprint* 1111.1553)
- [9] Abelev B *et al.* (ALICE) 2014 *Phys. Rev. Lett.* **113**(23) 232301 (*Preprint* 1405.3452)
- [10] Adam J *et al.* (ALICE) 2016 (*Preprint* 1605.07569)
- [11] Alioli S, Nason P, Oleari C and Re E 2010 *Journal of High Energy Physics* **2010** 1–58 ISSN 1029-8479
- [12] Cacciari M *et al.* 2012 *JHEP* **2012** 1–24 ISSN 1029-8479 (*Preprint* 1205.6344)
- [13] Hocker A and Kartvelishvili V 1996 *NIM* **A372** 469–481 (*Preprint* hep-ph/9509307)